UNCLASSIFIED

Australian Government

Department of Defence

Science and Technology

The Estimation of Uncertainty in Theoretical Corrections to Unsteady Pressure Measurements through Tubes

Jesse McCarthy and Malcolm Jones

Aerospace Division
Defence Science and Technology Group

DST-Group–TR–3579

ABSTRACT

A general method used to quantify uncertainty in theoretical corrections to unsteady pressure measurements through tubes is documented in this report. This method is based on a well-validated theoretical model, which produces a transfer function that may be used for correcting unsteady pressure measurements through an N_t number of tubes and N_v number of volumes. The uncertainty estimation methods employed are in accordance with AIAA Standards. A software tool, implementing a synthesis of the theoretical model and AIAA uncertainty estimation methodology, is also developed in this work. Aided by two separate case studies, it is found that by failing to account for uncertainty in the transfer function that is used to correct unsteady pressure data, the overall uncertainty in measured unsteady pressure may be misrepresented, depending on the spectral content of the measurements or tube configuration.

RELEASE LIMITATION

Approved for Public Release

UNCLASSIFIED

Produced by

Aerospace Division
506 Lorimer St,
Fishermans Bend, Victoria 3207, Australia

Telephone: 1300 333 362

June, 2019

APPROVED FOR PUBLIC RELEASE

The Estimation of Uncertainty in Theoretical Corrections to Unsteady Pressure Measurements through Tubes

Executive Summary

Measuring unsteady static pressure—that is, static pressure that varies rapidly with time—through tubes while not optimal, is sometimes necessary in fluid-dynamics testing. It is well known that unsteady pressure waves are modulated in amplitude and phase when travelling through tubes and, unless corrections are applied, the measurements will not represent the true quantities one expects.

A Linear Time-Invariant (LTI) transfer-function model was developed by Bergh & Tijdeman [1] to correct unsteady pressure amplitude and phase modulations through an N_t number of tubes and N_v number of volumes. It has previously been demonstrated that transfer-function corrections based on the theory in [1] agree excellently with experimental data, but are also sensitive to tube dimensions and mean ambient conditions. This sensitivity has led many to experimentally obtain transfer-function corrections for unsteady pressure measurements, rather than rely on theoretical models. While experimental corrections are advantageous in some situations, they are not always feasible for reasons of cost, time, or tubing configuration.

A general method for estimating uncertainty in the theoretical transfer function is reported here, which is based on the theory in [1] and is in accordance with AIAA Standards for uncertainty estimation [2]. Specifically, this methodology may be used to quantify the effect of uncertainty in the transfer function, due to uncertainties in tube dimensions and mean ambient conditions, on the overall uncertainty of unsteady pressure measurements. A software tool using this methodology is also developed and utilised in this work.

Two case studies presented here reveal that transfer-function uncertainty is highly sensitive to individual uncertainties in tube dimensions and moderately sensitive to mean ambient conditions. It is also found that by failing to account for uncertainty in the transfer-function parameters, the overall uncertainty in measured unsteady pressure may be misrepresented, depending on the spectral content of the measurements or tube configuration. Therefore, if measurements of unsteady pressure must be conducted through tubes, and theoretical transfer-function corrections are to be used, it is recommended that the methodology in this report be employed *a priori* to testing, so that the transfer-function uncertainty is known—or at least appreciated.

This page is intentionally blank

Contents

Figures

Tables

Glossary

AIAA	American Institute of Aeronautics and Astronautics
CLI	Command-Line Interface
CSV	Comma Separated Value
DPMS	Dynamic Pressure Measurement System
DFT	Discrete Fourier Transform
DST	Defence Science and Technology
GUI	Graphical User Interface
ID	Internal Diameter
IFT	Inverse Fourier Transform
IRF	Impulse Response Function
LTI	Linear Time-Invariant
NFFT	Number of Fast Fourier Transforms
RC	Resistor-Capacitor
RMS	Root-Mean-Square
RSS	Root-Sum-Square
RWT	Research Wind Tunnel
SSL	Standard Sea Level
TF	Transfer Function

Notation

$A(\nu)$	Amplitude spectrum
a_0	Mean velocity of sound, $\sqrt{\frac{\gamma p_s}{\rho_s}}$
B_i	Bias uncertainty in a measured variable y_i
B_r	Bias uncertainty in an experimental result r
$\overline{C_p}$	Mean pressure coefficient
$(C_p)_{\mathrm{RMS}}$	Root-Mean-Square pressure coefficient
c_p	Specific heat capacity at constant pressure
c_v	Specific heat capacity at constant volume
$H(\nu)$	Linearised transfer function
$\Im$	Imaginary part of complex number
i	$\sqrt{-1}$
J_n	Bessel function of the first kind, of nth order
K	Coverage factor
k	Polytropic constant
L	Tube length
M	Number of measured variables
N_i	Number of measurements or test replicates
N_t	Number of tubes
N_v	Number of volumes
n	$\left[1+\frac{\gamma-1}{\gamma}\frac{J_2\alpha\sqrt{Pr}}{J_0\alpha\sqrt{Pr}}\right]^{-1}$
P_i	Precision uncertainty in a measured variable y_i
P_r	Precision uncertainty in an experimental result r
Pr	Prandtl number, $\frac{\mu c_p}{\lambda}$
$\langle p \rangle$	Instantaneous local static pressure, $\overline{p}+p$
$\overline{p}$	Mean component of local static pressure
p	Unsteady component of local static pressure
p_{abs}	Absolute pressure
p_∞	Free-stream static pressure
p_R	Pitot-static tube reference static pressure
p_s	Mean ambient pressure
p_X	Pitot-static tube total pressure
q_∞	Free-stream dynamic pressure, $p_X - p_R$

$\Re$	Real part of complex number
R	Tube radius
R_0	Gas constant
r	Experimental result
$S(\nu)$	Power spectrum
S_i	Sample standard deviation of measured variable y_i
T	Sample period
T_s	Mean ambient temperature
t	Time
U_i	Total uncertainty in a measured variable, $\left({B_i}^2 + {P_i}^2\right)^{1/2}$
U_r	Total uncertainty in an experimental result, $\left({B_r}^2 + {P_r}^2\right)^{1/2}$
V_t	Tube volume, $\pi R^2 L$
V_v	Pressure transducer volume
w	A constant
y_i	Measured variable
$y(t)$	Function of time
$\overline{y_i}$	Sample mean of measured variable y_i

Greek Symbols

α	Shear wave number, $i\sqrt{i}R\sqrt{\frac{\rho_s \nu}{\mu}}$
γ	Specific heat ratio, $\frac{c_p}{c_v}$
θ	Hemisphere centre-line meridional angle
λ	Thermal conductivity
μ	Absolute (dynamic) fluid viscosity
ν	Frequency
ν_c	Nyquist (cut-off) frequency
ν_s	Sampling (quantisation) frequency
ρ_s	Mean density, $\frac{p_s}{R_0 T_s}$
σ	Dimensionless increase in transducer volume due to diaphragm deflection
ϕ	$\frac{\nu}{a_0}\sqrt{\frac{J_0 \alpha}{J_2 \alpha}}\sqrt{\frac{\gamma}{n}}$

Subscripts

m, i	Indices
j	jth tube or volume

1. Introduction

1.1. Context and Scope

Measurement of mean static pressure using pressure transducers, on the surface of a test article or in an off-body flow, is a standard capability in many fluid dynamics testing facilities. In general, a pressure tap is connected to the transducer via a single tube, or multiple tubes, with minimal concern regarding tube length(s), internal diameter(s) (ID) as well as configuration. This is because mean-pressure measurements are not significantly affected by the presence of tubing. However, this is not the case for measurements of unsteady pressure. In this context, "unsteady pressure" refers to the classical decomposition such that

$$\langle p \rangle = \overline{p} + p, \tag{1}$$

where $\langle p \rangle$ is the instantaneous pressure, $\overline{p}$ is the mean pressure component and p is the unsteady pressure component, or the pressure *disturbance*.

Unsteady pressure transducers (such as Kulites [3]) are usually installed directly on pressure taps, so as to avoid the use of tubes. However, with tests involving measurement of unsteady pressure at many locations, on actuated surfaces, or on test articles with complex geometries, financial considerations and/or geometric factors may dictate that measurements of unsteady pressure be done via tubes between the pressure taps and transducers—similar to measurements of mean pressure. Furthermore, many multi-holed unsteady pressure probes have some length of tube between the pressure taps and the transducers, so as to keep the probe sensing head as small as possible to spatially resolve the smaller scales in turbulent flows.

It is well known that a pressure disturbance propagating through tubes is subject to amplitude and phase modulation, due to boundary-layer induced viscous dissipation and the finite propagation velocity of the disturbance. For example, consider a three-tube, single-volume configuration, illustrated in Fig. 1. Such a configuration is commonly utilised for mean surface-pressure measurements. The pressure tap nearest to the flow (stations '0–1'), the tube attached to the transducer (stations '2–3'), as well as the tube between them (stations '1–2'), have unique radii R_j and lengths L_j. Now, when a pressure disturbance p occurs near station '0', it propagates through the tubes in the positive x direction, and ultimately enters

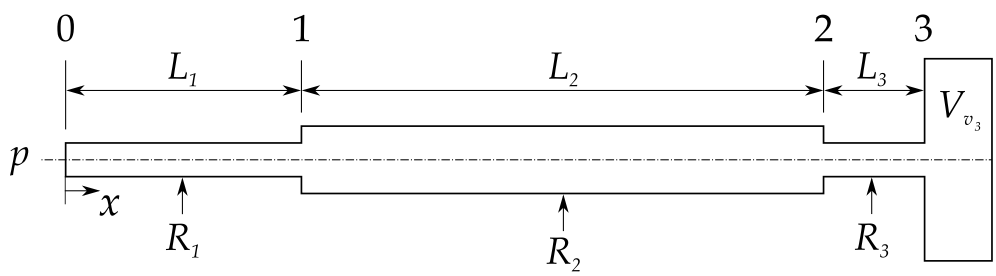

Figure 1: Illustration of an example three-tube, single-volume configuration for measuring a pressure disturbance.

the pressure transducer volume V_{v3} (station '3'). The propagation velocity of p through the tubes and different boundary conditions at each station causes the amplitude and phase of p at station '3' to distort relative to station '0'. Thus correction of measured p at station '3', to recover actual p at station '0', is required.

A theoretical Linear Time-Invariant (LTI) model was developed by Bergh & Tijdeman [1] to correct measured pressure disturbances through tubes, so as to recover the actual disturbances. The model is a generalised recursive-type equation used to determine the complex pressure ratio p_j/p_{j-1} for a series of N_t tubes and N_v volumes. The pressure disturbance p_j in tube or volume j and the disturbances in tubes or volumes $j-1$ and $j+1$ [1, Eq. (1)] are related as

$$\frac{p_j}{p_{j-1}} = \Bigg[\cosh(\phi_j L_j) + \frac{V_{v_j}}{V_{t_j}}\left(\sigma_j + \frac{1}{k_j}\right) n_j \phi_j L_j \sinh(\phi_j L_j) + \frac{V_{t_{j+1}} \phi_{j+1} L_j J_0 \alpha_j J_2 \alpha_{j+1}}{V_{t_j} \phi_j L_{j+1} J_0 \alpha_{j+1} J_2 \alpha_j} \frac{\sinh(\phi_j L_j)}{\sinh(\phi_{j+1} L_{j+1})}\left(\cosh(\phi_{j+1} L_{j+1}) - \frac{p_{j+1}}{p_j}\right)\Bigg]^{-1}. \quad (2)$$

Eq. (2) is the *transfer function*, which is a complex function, between the disturbances at two points separated by tubes and/or volumes. The derivation of Eq. (2) assumes that pressure disturbances are small compared to their mean value, thus permitting linearisation of the governing equations; see [1] for the complete derivation and list of model assumptions.

Decomposition of Eq. (2) into real $\Re\{p_j/p_{j-1}\}$ and imaginary $\Im\{p_j/p_{j-1}\}$ components allows for calculation of disturbance amplitude and phase modulation, as a function of disturbance input frequency ν. Letting p_j/p_{j-1} be defined as $H(\nu)_j$, it is not difficult to see for the three-tube single-volume example in Fig. 1 that the amplitude and phase responses are respectively given as

$$\left|\frac{p_3}{p_0}(\nu)\right| = \left[(\Re\{H(\nu)_1 \cdot H(\nu)_2 \cdot H(\nu)_3\})^2 + (\Im\{H(\nu)_1 \cdot H(\nu)_2 \cdot H(\nu)_3\})^2\right]^{\frac{1}{2}}, \quad (3)$$

$$\arg\left(\frac{p_3}{p_0}(\nu)\right) = \tan^{-1}\left(\frac{\Im\{H(\nu)_1 \cdot H(\nu)_2 \cdot H(\nu)_3\}}{\Re\{H(\nu)_1 \cdot H(\nu)_2 \cdot H(\nu)_3\}}\right). \quad (4)$$

That is, for each tube and/or volume in the system, there must be one transfer function that describes the amplitude and phase modulation of the disturbance propagating through that tube and/or volume. The overall transfer function between the pressure-disturbance source and measurement locations is then the product of each individual transfer function. In principle, by applying an Inverse Fourier Transform (IFT) to the overall transfer function, the Impulse Response Function (IRF) is obtained, and convolution of the IRF with the time series of measured disturbances recovers the time series of the actual disturbances. Alternatively, the overall transfer function may be multiplied with the Discrete Fourier Transform (DFT) of the measured time series data and subsequently transformed into temporal space via an IFT to recover the corrected time series.

1.2. Literature Survey

The theory in [1] has previously been applied for corrections to pressure disturbances through tubes and has been widely validated by others [4, 5, 6, 7]. Measurements have also been done at Defence Science and Technology (DST) using a Turbulent Flow Instrumentation® Dynamic Pressure Measurement System (DPMS), which incorporates the theory of [1] to correct measured disturbances through tubes. The DPMS was used to measure mean- and unsteady-pressure distributions on a vertical stabiliser experiencing vortex buffeting [8, 9]. The DPMS has also been used to measure unsteady pressure on a hemispherical protuberance [10, 11], see also the case study in Section 5 of this report. Similar unsteady pressure measurements on a hemisphere were done by Cheng & Fu [12], but using a Scanivalve® ZOC pressure measurement system; details of corrections to measurements were not reported. Others have disregarded any corrections to measured pressure fluctuations through tubes, and pneumatically tuned the tube configuration to have a flat amplitude response up to a certain frequency [13], but this resulted in a significantly reduced frequency response of the system (i.e. ≤ 300 Hz).

It has been shown both theoretically and experimentally by Bergh & Tijdeman [1] that the transfer function is most sensitive to L_j, R_j, mean ambient pressure p_s and mean ambient temperature T_s. While the transfer function is also dependent on dynamic viscosity μ, specific heat capacities c_v and c_p, thermal conductivity λ, and transducer volume changes σ—and derived results from these variables—their influences on the transfer function were found to be negligible [1]. Nevertheless, the sensitivity of the transfer function to L_j, R_j, p_s and T_s, as well as a lack of a standardised methodology to quantify uncertainty in the transfer function, has led many to alternatively obtain the transfer function through acoustic calibration. This approach may be advantageous in certain circumstances (e.g. see [14]). However: 1) it may be time consuming and costly to experimentally determine individual transfer functions for a large-channel configuration, 2) the calibration may introduce additional uncertainties while 3) still lacking information regarding uncertainties in p_s and T_s. Thus, the theoretical transfer function may be used instead to rapidly and accurately correct unsteady pressure data.

1.3. Objectives

The uncertainty in the theoretical transfer function, due to uncertainties in its independent variables, has not been previously quantified using a formal approach[1]. Therefore, a general methodology is presented that can be used to formally quantify the propagation of uncertainties in any variable, into the theoretical transfer function for an N_t-tube, N_v-volume configuration. Specifically however, the methodology in this report is restricted to propagating uncertainties in the variables L_j, R_j, p_s and T_s into the theoretical transfer function, so as to ultimately estimate the uncertainty in unsteady-pressure measurements through tubes. Herein, the term "transfer function" refers exclusively to the theoretical transfer function, unless stated otherwise.

[1]That is, the methodology is in accordance with a known standard and is not "abstract" in its approach.

2. Uncertainty Definitions

A standardised and exhaustive method for estimating uncertainty in wind-tunnel measurements is given by AIAA Standard S-071A-1999 [2]. Here, the uncertainty analysis is in accordance with the methodology recommended in [2] but for reference, key equations and concepts are summarised in the context of this study (see [2, Chap. 2] for more details). It should be noted that many other standards for uncertainty assessment exist, and each one could be used in place of [2] to similar effect.

2.1. Estimating Uncertainty in a Measured Variable

The total uncertainty $\pm U_i$ about a measured variable y_i is given by [2, Eq. (2-3)]

$$U_i = \left(B_i^2 + P_i^2\right)^{1/2}, \tag{5}$$

where B_i and P_i are the bias and precision uncertainties of y_i, respectively. The precision uncertainty P_i is determined for measurements of y_i as per [2, Eq. (2-4)], i.e.

$$P_i = KS_i, \tag{6}$$

where K is the coverage factor, equal to 2 for a 95% confidence level[2], and S_i is the sample standard deviation of N_i measurements of y_i [2, Eq. (2-5)]

$$S_i = \left(\sum_{m=1}^{N_i} \frac{\left[(y_i)_m - \overline{y_i}\right]^2}{N_i - 1}\right)^{1/2}, \tag{7}$$

where the sample mean of y_i is given by [2, Eq. (2-6)]

$$\overline{y_i} = \frac{1}{N_i}\sum_{m=1}^{N_i} (y_i)_m \,. \tag{8}$$

Eq. (6) is only used to determine P_i when the time intervals between measurements of y_i are insignificant compared to slowly varying changes in y_i over time—for example, N_i pressure samples taken at a sampling rate much higher than the rate of temperature drift in the pressure transducer. If *averaged* results of y_i from N_i test replicates are used to determine P_i, then the following equation should be used instead [2, Eq. (2-7)],

[2]It is recommended in [2] that unless there are extraneous circumstances dictating otherwise, a coverage factor of $K = 2$ should be used for reporting uncertainties.

$$P_{\overline{y}_i} = \frac{P_i}{\sqrt{N_i}}. \tag{9}$$

The bias uncertainty B_i may be taken from existing calibration or manufacturer's uncertainty data. For example, given a pressure transducer with a stated calibration uncertainty of ±7.5 Pa at 95% confidence, it is useful to assume that the calibration measurements conform to a normal statistical distribution with standard deviation b_i so that [2]

$$B_i = 2b_i, \tag{10}$$

which is analogous to Eq. (6) with $K = 2$. Using this assumption with the pressure transducer example, $b_i = B_i/2$ and thus $B_i = \pm 7.5$ Pa is used for propagating the calibration uncertainty into estimations of U_i.

If there are multiple contributions of bias uncertainty to the measurement of a single variable, then multiple bias uncertainties are combined as a root-sum-square (RSS) contribution to the total bias uncertainty for that variable. For example, consider a point measurement of total pressure p_X, in a non-uniform flow that has previously been calibrated to reveal variability of ±20 Pa in the plane of measurement. The bias uncertainty B_1 of the pressure transducer *and* the bias uncertainty B_2 in acquiring a point pressure measurement in a non-uniform flow contribute to the total bias uncertainty B_{p_X} in the measurement of p_X as

$$B_{p_X} = \left(B_1^2 + B_2^2\right)^{1/2}. \tag{11}$$

B_i and P_i must be calculated for every measured variable y_i that significantly influences derived experimental results, as discussed in the next section.

2.2. Estimating Uncertainty in an Experimental Result

Total uncertainty $\pm U_r$ about an experimental result r occurs through some reduction equation comprised of M measured variables so that $r = f\left(y_1, y_2, y_3, \ldots, y_M\right)$. A common example is the mean pressure coefficient

$$\overline{C_p} = \frac{\overline{p} - p_\infty}{q_\infty}, \tag{12}$$

where $\overline{p}$ is the local mean static pressure measured by a pressure transducer, p_∞ is the free-stream static pressure measured by a possibly different transducer to $\overline{p}$, and q_∞ is the free-stream dynamic pressure measured by a possibly different transducer to $\overline{p}$ and p_∞. It can then be seen in Eq. (12) that uncertainty in each measured variable propagates through to an uncertainty in $\overline{C_p}$.

Similarly to Eq. (5), U_r is defined as per [2, Eq. (2-9)], i.e.

$$U_r = \left(B_r^2 + P_r^2\right)^{1/2}, \tag{13}$$

where B_r and P_r are the bias and precision uncertainties of the result r. If only one test replicate has been performed, P_r is estimated from M measured variables as per [2, Eq. (2-13)],

$$P_r^2 = \sum_{i=1}^{M} \left(\frac{\partial r}{\partial y_i} P_i\right)^2. \tag{14}$$

The partial derivatives are known as the *sensitivity coefficients*, and they quantify the sensitivity of the reduction equation to uncertainty in each measured variable. B_r is determined from M bias uncertainties of measured variables as [2, Eq. (2-16)]

$$B_r^2 = \left[\sum_{i=1}^{M} \left(\frac{\partial r}{\partial y_i} B_i\right)^2\right] + 2\frac{\partial r}{\partial y_a}\frac{\partial r}{\partial y_b} {B_a}' {B_b}', \tag{15}$$

where perfectly correlated uncertainties ${B_a}'$ and ${B_b}'$ in variables y_a and y_b, measured using instruments calibrated to the same working standard, are limited to the uncertainty of that working standard. Using the example in Eq. (12), if two absolute pressure transducers are used to give nominal measures of $\overline{p} = 95,000$ Pa and $p_\infty = 97,000$ Pa, and they are both calibrated against the same working standard that has an uncertainty of $\pm(3 + [0.00004 p_{abs}])$ Pa where p_{abs} is the absolute pressure measurement, then

$$\begin{aligned} {B_{\overline{p}}}' &= 3 + (0.00004 \times 95000) = \pm 6.8 \text{ Pa; and} \\ {B_{p_\infty}}' &= 3 + (0.00004 \times 97000) = \pm 6.9 \text{ Pa} \end{aligned}$$

If all measured variables are statistically uncorrelated, the corollary is that the correlated bias terms in Eq. (15) are equal to zero. It should also be noted that correlated bias uncertainties, depending on the sign of the sensitivity coefficients, can actually reduce the bias uncertainty of an experimental result.

3. Generalised Methodology

3.1. Overview

The principles in Section 2 are applied to estimations of uncertainty in the transfer function (Eq. 2) due to uncertainties in tube dimensions and ambient conditions, according to the following generalised method:

1. Determine the tube configuration (N_t tubes, N_v volumes) used in unsteady pressure measurements;

2. Derive the transfer function $H(\nu)$ using Eq. (2) for the tube configuration. The transfer function $H(\nu)$, in this case, is the reduction equation used to obtain the result r;

3. Determine nominal values for each variable in $H(\nu)$;

4. Determine B_i and P_i for each variable: tube lengths L_j, tube radii R_j, mean pressure p_s and temperature T_s (Section 2.1);

5. Determine B_r and P_r of $H(\nu)$, accounting for any correlated bias uncertainties if necessary (Section 2.2);

6. Determine U_r of $H(\nu)$ and report uncertainty bounds on nominal amplitude and phase responses, as well as the corrected time-series data.

This method is explained in the following section for the three-tube, single-volume example in Fig. 1. A software tool was also developed so that the nominal amplitude and phase responses, as well as their uncertainties, could be determined using this generalised approach. Further details on this software tool are documented in Appendix A.

3.2. Example Uncertainty Analysis

3.2.1. Step 1: Determine the tube configuration used in unsteady pressure measurements

The tube configuration consists of three tubes of differing but known lengths and radii, followed by a pressure transducer volume. While Eq. (2) assumes perfectly straight tubes of infinite rigidity, moderate curvature in the tubing, as well as tube material, seem to insignificantly affect the transfer-function fidelity [1, 5, 8]. However, “kinks”—that is, extreme tube curvature to the point of deformation and blockage—should be avoided because of adverse effects on transfer-function fidelity. It is also assumed for this example that air is the working fluid.

3.2.2. Step 2: Derive the transfer function for the specific tube configuration

The pressure disturbance acts at station ‘0’ and propagates through to station ‘3’. Thus the overall transfer function to be determined is p_3/p_0 and is obtained as

$$\frac{p_3}{p_0} = H(\nu) = \frac{p_1}{p_0} \cdot \frac{p_2}{p_1} \cdot \frac{p_3}{p_2}. \tag{16}$$

Inspection of Eq. (2) reveals that it may be more convenient to start the derivation at the transducer volume location (station '3'), since $j + 1$ terms are present and will be identically zero since there are no further tubes or volumes beyond the transducer volume. Then, it follows that

$$\frac{p_3}{p_2} = \left[\cosh(\phi_3 L_3) + \frac{V_{v_3}}{V_{t_3}} \cancelto{1}{\left(\sigma_3 + \frac{1}{k_3}\right)} n_3 \phi_3 L_3 \sinh(\phi_3 L_3)\right]^{-1}. \tag{17}$$

The term $\left(\sigma + \dfrac{1}{k}\right)$ is assumed to be unity throughout this derivation, as well as in the DST software tool (Appendix A). This is because it was shown in experiments by Bergh & Tijdeman [1] that σ is a small number, thus $\sigma \approx 0$; also, the polytropic constant k of air generally varies in the range $1 \leq k \leq 1.4$. Subsequently,

$$\begin{aligned} \frac{p_2}{p_1} = \Bigg[\cosh(\phi_2 L_2) + \cancelto{0}{\frac{V_{v_2}}{V_{t_2}}} n_2 \phi_2 L_2 \sinh(\phi_2 L_2) + \\ \frac{V_{t_3} \phi_3 L_2 J_0 \alpha_2 J_2 \alpha_3}{V_{t_2} \phi_2 L_3 J_0 \alpha_3 J_2 \alpha_2} \frac{\sinh(\phi_2 L_2)}{\sinh(\phi_3 L_3)} \left(\cosh(\phi_3 L_3) - \frac{p_3}{p_2}\right)\Bigg]^{-1}, \end{aligned} \tag{18}$$

where $V_{v_2} = 0$ because there is a discontinuity in tube radius at station '2', rather than a volume. Finally,

$$\begin{aligned} \frac{p_1}{p_0} = \Bigg[\cosh(\phi_1 L_1) + \cancelto{0}{\frac{V_{v_1}}{V_{t_1}}} n_1 \phi_1 L_1 \sinh(\phi_1 L_1) + \\ \frac{V_{t_2} \phi_2 L_1 J_0 \alpha_1 J_2 \alpha_2}{V_{t_1} \phi_1 L_2 J_0 \alpha_2 J_2 \alpha_1} \frac{\sinh(\phi_1 L_1)}{\sinh(\phi_2 L_2)} \left(\cosh(\phi_2 L_2) - \frac{p_2}{p_1}\right)\Bigg]^{-1}. \end{aligned} \tag{19}$$

3.2.3. Step 3: Determine nominal values for each variable in $H(\nu)$

Once $H(\nu)$ has been derived in Section 3.2.2, the nominal value for each variable is required. For variables p_s and T_s, these could be values at the test conditions of interest to the uncertainty

Table 1: Constants for Eqs. (20), (22) and (23).

Constant	Eq. (20) [15]	Eq. (22) [16]	Eq. (23) [16]
w_1	1.009950160×10^4	33.9729025	3.12013125
w_2	1.968275610×10^2	-1.64702679×10^2	-23.0762400
w_3	5.009155110	2.62108546×10^2	1.65049430
w_4	$5.761013730 \times 10^{-3}$	-21.5346955	-0.191148175
w_5	$1.066859930 \times 10^{-5}$	-4.43455815×10^2	–
w_6	$7.940297970 \times 10^{-9}$	6.07339582×10^2	–
w_7	$2.185231910 \times 10^{-12}$	-3.68790121×10^2	–
w_8	–	1.11296674×10^2	–
w_9	–	-13.4122465	–

analysis. Variables L_j and R_j may be measured before testing[3], $V_{t_j} = \pi {R_j}^2 L_j$, and V_{v_j} of the pressure transducer may usually be determined from manufacturer's specifications.

The specific heat capacity of air at constant pressure c_p may be calculated as a function of T_s (for $200 \leq T_s \leq 1000$ K) as per [15], i.e.

$$c_p = R_0 \left[\left(\frac{w_1}{T_s^2} \right) + \left(\frac{w_2}{T_s} \right) + (w_3) + (w_4 T_s) + \left(w_5 T_s^2 \right) + \left(w_6 T_s^3 \right) + \left(w_7 T_s^4 \right) \right], \tag{20}$$

where the constants $w_{1,2,\ldots,7}$ are defined in Table 1 and the gas constant for dry air $R_0 = 287.04$ J/kg·K. The mean density of air ρ_s may be determined using the ideal gas law,

$$\rho_s = \frac{p_s}{R_0 T_s}. \tag{21}$$

The thermal conductivity of air λ may be calculated as a function of T_s and ρ_s, using kinetic theory [16], i.e.

$$\begin{aligned} \lambda_{T_s} = 0.004358 \Bigg[& \left(w_1 \left(\frac{T_s}{132.52} \right)^{-1} \right) + \left(w_2 \left(\frac{T_s}{132.52} \right)^{-\frac{2}{3}} \right) + \left(w_3 \left(\frac{T_s}{132.52} \right)^{-\frac{1}{3}} \right) + \\ & (w_4) + \left(w_5 \left(\frac{T_s}{132.52} \right)^{\frac{1}{3}} \right) + \left(w_6 \left(\frac{T_s}{132.52} \right)^{\frac{2}{3}} \right) + \left(w_7 \left(\frac{T_s}{132.52} \right) \right) + \\ & \left(w_8 \left(\frac{T_s}{132.52} \right)^{\frac{4}{3}} \right) + \left(w_9 \left(\frac{T_s}{132.52} \right)^{\frac{5}{3}} \right) \Bigg], \end{aligned} \tag{22}$$

[3] In [1], various methods are given by which to calculate an "effective" value of R for each tube, instead of using nominal dimensions from manufacturer's data; these methods are rigorous, and are not documented here.

$$\lambda_{\rho_s} = 0.004358\left[\left(w_1\frac{\rho_s}{313}\right) + \left(w_2\left(\frac{\rho_s}{313}\right)^2\right) + \left(w_3\left(\frac{\rho_s}{313}\right)^3\right) + \left(w_4\left(\frac{\rho_s}{313}\right)^4\right)\right], \tag{23}$$

$$\lambda = \lambda_{T_s} + \lambda_{\rho_s}, \tag{24}$$

where the constants in Eqs. (22) and (23) are *different* than in Eq. (20) and are included in Table 1. The dynamic viscosity μ may be calculated as a function of T_s using Sutherland's formula [17],

$$\mu = \frac{1.458 \times 10^{-6} \times (T_s)^{1.5}}{T_s + 110.4}. \tag{25}$$

Once Eqs. (20), (21), (24) and (25) have been used to compute c_p, ρ_s, λ and μ respectively, it follows that the mean velocity of sound a_0 and the Prandtl number Pr may be determined as

$$a_0 = \sqrt{\frac{\gamma p_s}{\rho_s}}, \tag{26}$$

where $\gamma = 1.4$ for air, and

$$Pr = \frac{\mu c_p}{\lambda}. \tag{27}$$

Up to this point, all the calculated parameters are independent of disturbance input frequency ν. Now, quantities dependant on ν are calculated. The shear wave number of the jth tube α_j is calculated as

$$\alpha_j = i\sqrt{i}R_j\sqrt{\frac{\rho_s \nu}{\mu}}. \tag{28}$$

Then, the parameter ϕ_j is determined as

$$\phi_j = \frac{\nu}{a_0}\sqrt{\frac{J_0\alpha_j}{J_2\alpha_j}}\sqrt{\frac{\gamma}{n_j}}, \tag{29}$$

where

$$n_j = \left[1 + \frac{\gamma - 1}{\gamma} \frac{J_2 \alpha_j \sqrt{Pr}}{J_0 \alpha_j \sqrt{Pr}}\right]^{-1}, \tag{30}$$

and J_0, J_2 are Bessel functions of the first kind of zeroth and second order, respectively.

Once all nominal variable values are calculated, $H(\nu)$ may be computed as a function of ν, with amplitude and phase determined according to Eqs. (3) and (4) respectively.

3.2.4. Step 4: Determine B_i and P_i for L_j, R_j, p_s and T_s

The bias and precision uncertainties in each variable are determined using the standardised methodology in Section 2.1. This is generally straightforward for p_s and T_s, where calibration data and time-series of measurements are usually available. However, this may not be straightforward for uncertainties in variables L_j and R_j.

In this example, there are three different tubes between the locations of the pressure disturbance and the transducer. In principle, there should be one bias (B_{L_i}, B_{R_i}, $i = 1, \ldots, 3$) and one precision (P_{L_i}, P_{R_i}, $i = 1, \ldots, 3$) uncertainty associated with each individual tube for each variable (L and R). However, bias and/or precision uncertainty estimations for each tube may not be readily available—in which case they might be estimated through metrology, engineering judgement on the basis of prior knowledge, or simply neglected[4]. For the purposes of this example, the dimensional tolerances of L_1, L_3 and R_1, R_3, i.e. the bias uncertainties B_{L_1}, B_{L_3} and B_{R_3}, B_{R_3}, are known from manufacturer's data, but their precision uncertainties are unknown.

Often, a flexible tube connects the pressure tap to the transducer. This tube is cut to a pre-specified length, depending on experimental set-up requirements. In this case bias uncertainty B_{L_2}, which is usually derived from manufacturing tolerances, may be more appropriately derived from calibration data of the length-measurement device, such as a calliper or steel rule. Precision uncertainty P_{L_2} could then be determined from the standard deviation of N_i tube length measurements (Eq. 6), or estimated using engineering judgement.

Bias uncertainty B_{R_2} in tube radius could come from manufacturing tolerances, or engineering judgement. However, estimation of precision uncertainty P_{R_2} is difficult, as it is essential to have N_i measurements of tube internal diameter. The sensitivity of the transfer function to R_j necessitates development of a robust method by which to accurately measure R_j—especially for small, flexible tubes; but it is presently outside the scope of this report to develop this methodology.

3.2.5. Step 5: Determine B_r and P_r of $H(\nu)$

The bias and precision uncertainties in $H(\nu)$ are now estimated using the standardised methodology outlined in Section 2.2. The bias uncertainty $B_{H(\nu)}$ is estimated as

[4] It is demonstrated in Section 4 that neglecting uncertainties in tube dimensions has considerable effect on transfer-function uncertainty and should be avoided if possible.

$$B_{H(\nu)}{}^2 = \left[\sum_{i=1}^{3} \left(\frac{\partial H(\nu)}{\partial L_i} B_{L_i} \right)^2 + \sum_{i=1}^{3} \left(\frac{\partial H(\nu)}{\partial R_i} B_{R_i} \right)^2 + \left(\frac{\partial H(\nu)}{\partial p_s} B_{p_s} \right)^2 + \left(\frac{\partial H(\nu)}{\partial T_s} B_{T_s} \right)^2 \right] + \text{correlated terms}, \quad (31)$$

where on the basis of complicatedness, the correlated bias terms are neglected for this example. Similarly, precision uncertainty $P_{H(\nu)}$ is estimated as

$$P_{H(\nu)}{}^2 = \left[\sum_{i=1}^{3} \left(\frac{\partial H(\nu)}{\partial L_i} P_{L_i} \right)^2 + \sum_{i=1}^{3} \left(\frac{\partial H(\nu)}{\partial R_i} P_{R_i} \right)^2 + \left(\frac{\partial H(\nu)}{\partial p_s} P_{p_s} \right)^2 + \left(\frac{\partial H(\nu)}{\partial T_s} P_{T_s} \right)^2 \right]. \quad (32)$$

The transfer function sensitivity coefficients in Eqs. (31) and (32) are highly complicated and may be derived exactly using a symbolic mathematics engine, or determined numerically using a finite differencing (or equivalent) algorithm.

3.2.6. Step 6: Determine U_r of $H(\nu)$

The bias $B_{H(\nu)}$ and precision $P_{H(\nu)}$ uncertainties calculated in Section (3.2.5) are functions of ν, thus the total uncertainty in the transfer function $U_{H(\nu)}$ is readily calculated, for each value of ν, as

$$U_{H(\nu)} = \left(B_{H(\nu)}{}^2 + P_{H(\nu)}{}^2 \right)^{1/2}. \quad (33)$$

It should be noted that for a complex number $z = x + iy$,

$$z^2 = x^2 - y^2 + 2ixy$$

and

$$\sqrt{z} = \sqrt{|z|} e^{i \frac{\arg(z)}{2}}.$$

The relationship between total uncertainty in the transfer function, and resultant uncertainty in the corrected unsteady pressure data, is discussed in the following two case studies, whereby practical application of this methodology is employed for:

1. A simulated unsteady pressure signal, and
2. Real unsteady pressure signals from DST wind-tunnel tests.

4. Case Study I: Simulated Fluctuating Signal

4.1. Overview

In order to demonstrate the generalised method outlined in Section 3, a software-simulated unsteady signal with known properties is generated as an input to the three-tube, single volume system described in Fig. 1. In this case study, the output (or measured) signal is being *predicted* using the transfer function, rather than the output signal being *corrected* to recover the input signal, but the methodology of estimating transfer-function uncertainty is invariant between both scenarios.

To clearly delineate the effects of uncertainties in transfer function parameters, as well as preserve the assumption of system linearity [1], the simulated signal is chosen to be both noiseless (i.e. uncorrupted), and small-amplitude relative to a mean value. Therefore, a linear superposition of sinusoids with cascading amplitudes and monotonically increasing frequencies is arbitrarily chosen to represent the input unsteady signal

$$y(t) = \left(\frac{5}{100}\sin\left(2\pi\nu_1 t\right)\right) + \left(\frac{25}{1000}\sin\left(2\pi\nu_2 t\right)\right) + \left(\frac{1}{100}\sin\left(2\pi\nu_3 t\right)\right) + \left(\frac{5}{1000}\sin\left(2\pi\nu_4 t\right)\right), \tag{34}$$

where $\nu_{1\ldots4}$ corresponds to 50, 250, 450 and 650 Hz respectively and t is time. Eq. (34) is quantised at a sampling frequency $\nu_s = 2,500$ Hz for a total period $T = 60$ seconds, similarly to the second case study in Section 5. The input signal is displayed in the time and frequency domains in Fig. 2, where $\nu_c = \nu_s/2$ the Nyquist (or cut-off) frequency and $A(\nu) = \sqrt{S(\nu)}$ the linear amplitude spectrum, which is the square-root of the power spectrum $S(\nu)$.

4.2. Methodology Application and Results

Step 1 (Section 3.2.1) requires specification of the tube configuration. The second case study documented in Section 5 involves unsteady pressure measurements on a hemisphere in a wind tunnel and so for direct comparison, the same tubing configuration in that study is used in this case study (see Fig. 11).

Step 2 (Section 3.2.2) requires derivation of the overall transfer function for the specified tube configuration. This is done using the DST software tool (Appendix A) for Standard Sea Level (SSL) conditions ($p_s = 101,325$ Pa and $T_s = 288.15$ K), with the result shown in Fig. 3. It can be seen that $|H(\nu)| \approx 0.5$ at ν_c. For a noiseless input signal such as the one in this case study, there is no risk of amplifying spurious noise at higher frequencies and so the transfer function may be used to correct the data up to and including the cut-off frequency. However, spurious noise amplification via the transfer function remains a risk for real measurements, and so careful consideration as to the limit of transfer-function applicability is required. It has been suggested that the transfer function corrections should only be applied up to the lesser of either the cut-off frequency, or the frequency at which the amplitude ratio is 0.4 [18]. It is also important to note the peak $|H(\nu)| \approx 1.6$ at about 130 Hz in Fig. 3, which means that

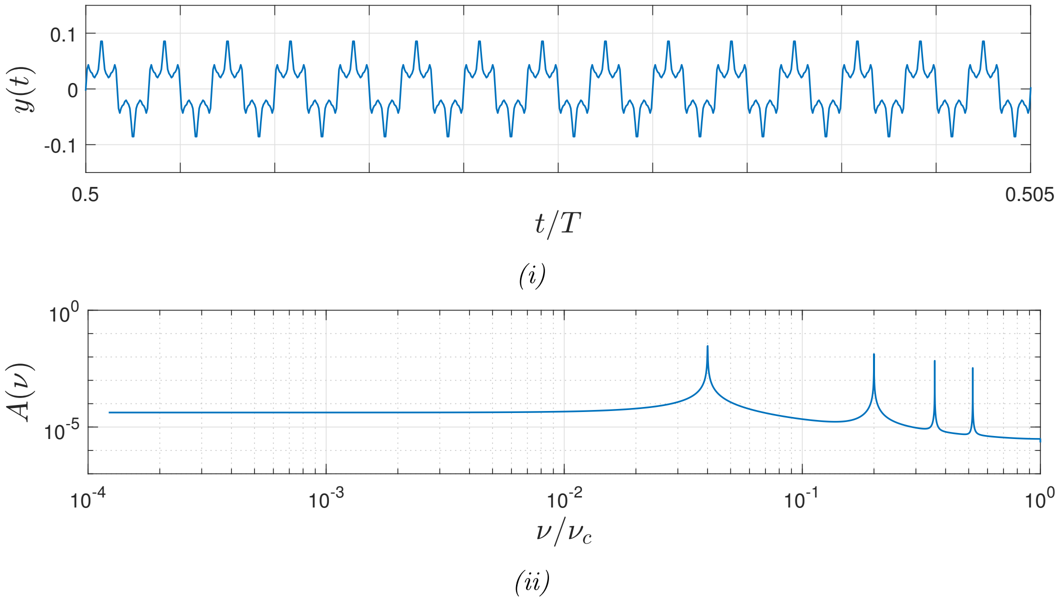

Figure 2: Simulated input signal in Eq. (34) represented in (i) time (enlarged window) and (ii) frequency domains, for case-study I.

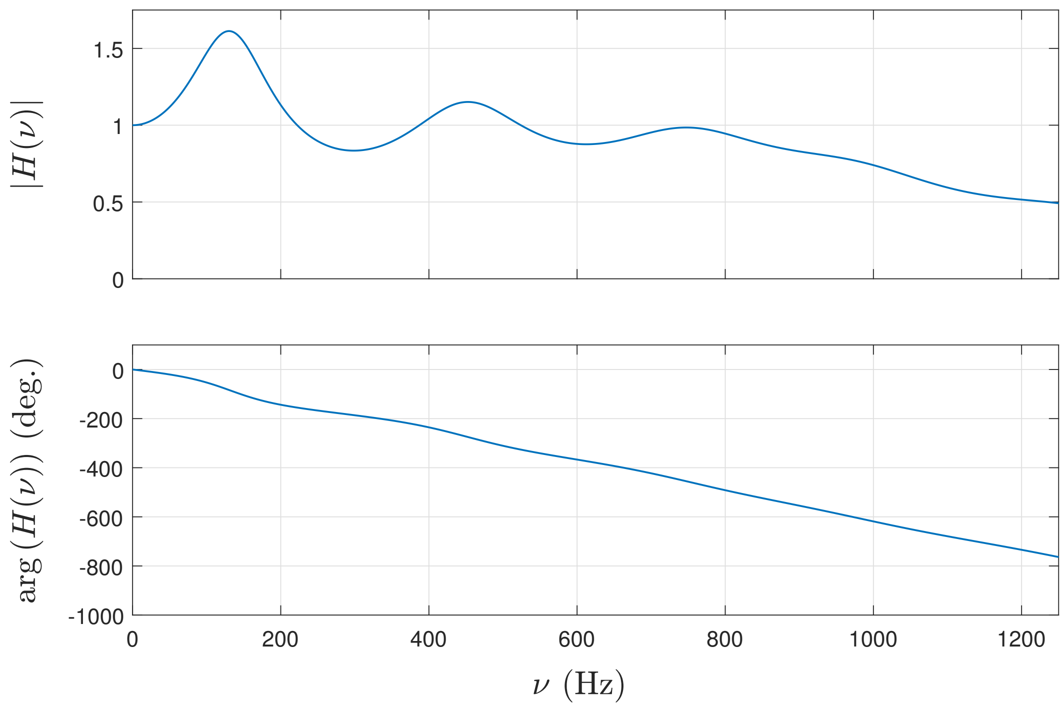

Figure 3: DST software-based transfer function estimate to $\nu_c = 1,250$ Hz for case-study I.

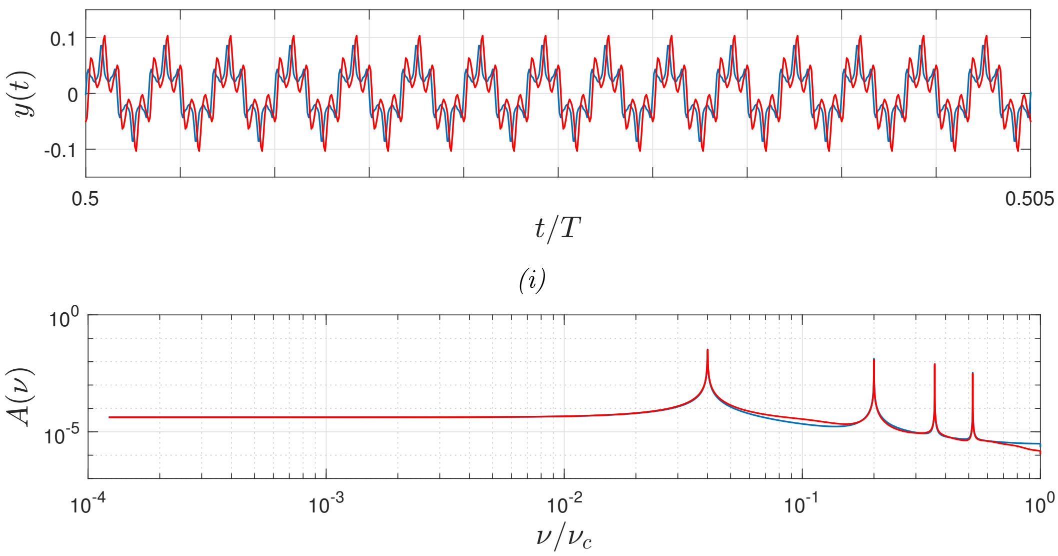

(ii)

Figure 4: (—) Output signal resulting from convolution of the (—) simulated input signal and derived transfer function, represented in (i) time (enlarged window) and (ii) frequency domains, for case-study I.

the tube configuration significantly amplifies the pressure disturbance at that frequency. The magnitude of these amplifications should be identified prior to testing, since it is possible to over-range the pressure transducer at the frequencies of these peaks.

In order to acquire the output signal, DFT convolution of $y(t)$ (consisting of 150,000 discrete samples) with a 2,048-point discretisation of $H(\nu)$ is carried out in the frequency domain using the overlap-save method [19]. The output signal in the time and frequency domains is shown in Fig. 4.

Step 3 (Section 3.2.3) requires that all nominal values of each parameter are known. The DST software tool uses Eqs. (20) to (30) to determine nominal values, in the domain of ν, from knowledge of p_s and T_s. For brevity, these nominal values are not documented but here they are computed for SSL conditions and $0 < \nu \leq \nu_c$. The nominal values for each tube and volume dimension are identical to those in the second case study.

Step 4 (Section 3.2.4) involves the estimation of uncertainties in L_1, R_1 to L_3, R_3, p_s and T_s. For consistency, the values estimated in the second case study, which are outlined in Table 6, are used in this case study.

Step 5 (Section 3.2.5) involves computing the sensitivity coefficients and hence determining $B_{H(\nu)}$ and $P_{H(\nu)}$ in the transfer function. The DST software tool does this internally using symbolic partial differentiation of the derived transfer function with respect to L_j, R_j, p_s and T_s (Appendix A). Given three tubes in this system, there are eight sensitivity coefficients to be determined and $B_{H(\nu)}$ and $P_{H(\nu)}$ are given by Eqs. (31) and (32) respectively as a function of ν. Note that correlated bias terms are neglected, as in Section 3.2.5.

Step 6 (Section 3.2.6) involves calculating $U_{H(\nu)}$ in the transfer function using Eq. (13). The DST software tool calculates $U_{H(\nu)}$ as a function of ν, and plots $\left|H(\nu) \pm U_{H(\nu)}\right|$ for amplitude response and $\arg\left(H(\nu) \pm U_{H(\nu)}\right)$ for phase response. The amplitude- and phase-response uncertainties of the derived transfer function are shown graphically in Fig. 5 and documented for specific values of ν in Table 2. Herein, the upper confidence bounds in amplitude and phase uncertainty are defined as $\left|H(\nu) + U_{H(\nu)}\right|$ and $\arg\left(H(\nu) + U_{H(\nu)}\right)$ respectively, while the lower bounds are likewise defined as $\left|H(\nu) - U_{H(\nu)}\right|$ and $\arg\left(H(\nu) - U_{H(\nu)}\right)$ respectively. This definition is necessary because it will be seen that upper and lower confidence bounds can cross-over multiple times in the domain of ν.

4.3. Discussion

4.3.1. Transfer Function Uncertainty Trends with Frequency

There are some key observations regarding amplitude- and phase-response uncertainties that warrant discussion. Firstly, it is important to note that when $\nu = 0$, the transfer function is undefined. This limit corresponds to the effect of tubes on the mean pressure component which, as initially discussed in Section 1, is insignificant. However, to avoid singularities in the numerics this limit is handled by forcing the amplitude response to be unity and phase response to be zero when $\nu = 0$, which is physically tantamount to the mean-pressure condition. Likewise, the transfer-function uncertainty at $\nu = 0$ is a numerical singularity, but on the basis of physical considerations, the uncertainty in amplitude and phase response are each forced to zero when $\nu = 0$.

It can be seen that the transfer-function uncertainty bounds in Fig. 5 represent modulated versions of the nominal transfer function; i.e., uncertainties in L_j, R_j, p_s and T_s cause the transfer function to change shape with ν. The upper and lower amplitude and phase confidence bounds also cross-over multiple times as ν increases; at these cross-over frequencies, transfer-function uncertainty is a local minimum but not identically zero, since the confidence-bound values at cross-over are close but not necessarily equal to the nominal transfer function values. To further understand the amplitude- and phase-uncertainty trends in Fig. 5, all eight sensitivity coefficients are decomposed into their respective amplitude and phase components, and plotted as a function of ν in Fig. 6; by doing so, this elucidates the relative influences of L_j, R_j, p_s and T_s on the transfer function[5]. The data plotted in Fig. 6 may be considered to be the *response characteristic* of the tube configuration.

Immediately noticeable in Fig. 6 is the large sensitivity of amplitude response to tube radii, given by the relatively large values of $\partial H(\nu)/\partial R_j$. This result agrees with findings in [1] and confirms the postulations of others (e.g. [14]). However, it is interesting to note the relatively small influence of p_s on the amplitude response, which suggests that large uncertainty in p_s must exist before there is any appreciable effect on the transfer function. Bergh & Tijdeman [1] suggested that changes in p_s had a considerable effect on the transfer function—albeit less than tube radii—but they made this statement based on large variations in p_s, on the order of ± 50 kPa, which are much larger than typical measurement uncertainty. Uncertainty in T_s appears to have a more pronounced effect on the transfer function than p_s, but is still nearly

[5]Here, the actual values of the sensitivity coefficients are somewhat meaningless compared to their values relative to each other.

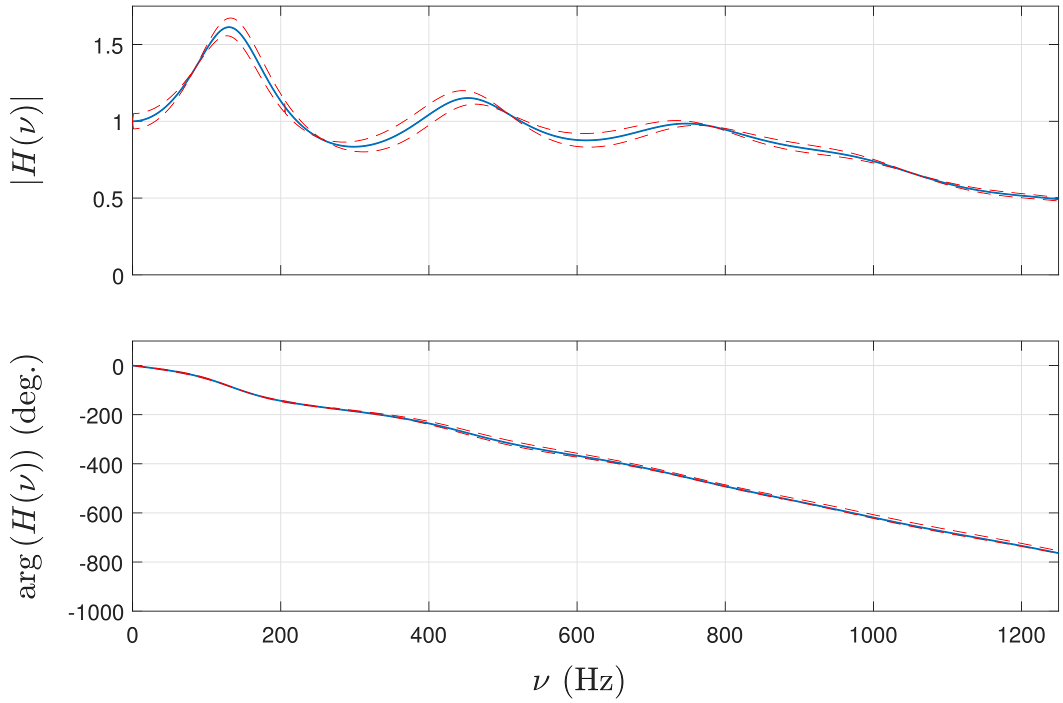

Figure 5: (– –) Total uncertainty at 95% confidence in (—) amplitude and phase responses, due to uncertainties in L_j, R_j, p_s and T_s, as a function of ν for case-study I.

Table 2: Total uncertainty bounds at 95% confidence in amplitude and phase responses, due to uncertainties in L_j, R_j, p_s and T_s, at discrete values of ν for case-study I.

ν (Hz)	$\lvert H(\nu)\rvert$	$\lvert H(\nu)+U_{H(\nu)}\rvert$ $\lvert H(\nu)-U_{H(\nu)}\rvert$	$\arg(H(\nu))$ (deg.)	$\arg(H(\nu)+U_{H(\nu)})$ $\arg(H(\nu)-U_{H(\nu)})$ (deg.)
250	0.896	0.902 0.895	−167.24	−162.51 −172
500	1.070	1.067 1.077	−310.19	−313.36 −307.06
1000	0.740	0.729 0.752	−618.44	−619.84 −617.08

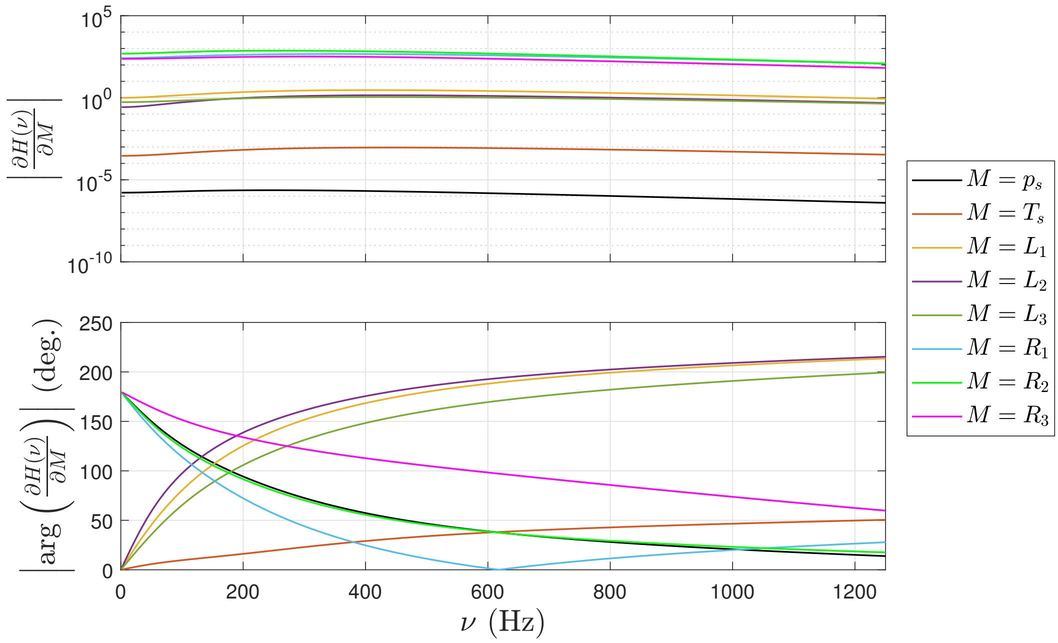

Figure 6: Sensitivity coefficients for case-study I amplitude and phase responses. Note the logarithmic ordinate scale for the amplitude-response sensitivities.

three orders of magnitude less influential than uncertainties in L_j. Though not the subject of this present investigation, this result suggests that temperature drift during wind-tunnel testing is likely to have negligible effect on transfer-function fidelity.

The response characteristic in Fig. 6 also reveals that local maxima occur in each sensitivity coefficient. It is presently unclear as to why these maxima occur, but it is probable that their occurrence—as well as location in the frequency spectrum—is highly dependent upon tube configuration. Nevertheless, the influence of uncertainties in L_j, R_j, p_s and T_s on amplitude response decreases as ν increases, which accounts for the decrease in amplitude uncertainty with ν in Fig. 5. The rate at which the sensitivity decreases is also likely a consequence of the tube configuration. It should be noted that even at large ν (not displayed), the amplitude-response sensitivity to all variables continued to decrease towards zero. Physically, this phenomenon could be explained as follows: the presence of tubes significantly attenuates the higher-frequency content of the unsteady pressure signal, as predicted by the transfer function in Fig. 3 (i.e. where $|H(\nu)| < 1$); this is mostly because of viscous dissipation due to the internal boundary layer in the tubes. Since significant attenuation of the smaller fluctuating scales is already occurring, there is less sensitivity of this attenuation to any global changes in variables L_j, R_j, p_s and T_s at the higher frequencies.

The absolute value of the phase components of the sensitivity coefficients are also plotted in Fig. 6. It is evident that the phase sensitivity is dependent on the frequency content of the unsteady pressure measurements, similar to the amplitude response. However, the phase response is more sensitive to the relative magnitudes in uncertainties between L_j, R_j, p_s and T_s, as compared to the amplitude response. For instance, the phase response is more sensitive to uncertainty in R_3 than R_2 for $\nu \leq \nu_c$, and uncertainty in R_2 affects phase response more than R_1 only for $\nu \lesssim 1{,}000$ Hz. Another remarkable observation in Fig. 6 is the mutually opposing effects of phase-response sensitivity to tube length and radius (with the exception of R_1 for $\nu \gtrsim 600$ Hz), and mean pressure and temperature. At frequencies below 50 Hz for this response characteristic, the phase response is most sensitive to uncertainties in R_j and p_s; however, as ν increases, uncertainties in L_j and T_s exert more influence on phase response. At $\nu \approx 205$ Hz, there is a local maximum in the sum of the phase sensitivity coefficients, which interestingly corresponds to a small discontinuity, which is barely visible in Fig. 5, in amplitude and phase uncertainty at $\nu \approx 205$ Hz. This discontinuity is related to the location of the complex argument of $U_{H(\nu)}$ on real-imaginary axes; since the real part $\Re\{U_{H(\nu)}\} \geq 0 \; \forall \; \nu$, any increase in $\arg\left(U_{H(\nu)}\right)$ above $\pi/2$ rad (90°) results in a quadrant (i.e. sign) change from the first to fourth quadrant, and *vice versa*. This sign change is therefore not related to any specific physical phenomenon, and is ostensibly inconsequential to amplitude- and phase-response uncertainty estimations.

In summary, the response characteristic is unique to the tube configuration, and may be used to display the relative influences of variables L_j, R_j, p_s and T_s on the amplitude- and phase response with varying ν. This is important to the uncertainty analysis; if the unsteady-pressure frequencies of interest are known *a priori* to testing, then the response characteristic gives insights into the most influential variables at those frequencies.

4.3.2. Transfer Function Uncertainty Trends with Varying Input Uncertainties

Now, uncertainties in L_j, R_j, p_s and T_s are varied and the effects of this variation on the uncertainty bounds in the amplitude and phase responses are examined. Recall the definitions:

$$B_{H(\nu)}{}^2 = \left[\sum_{i=1}^{3}\left(\frac{\partial H(\nu)}{\partial L_i}B_{L_i}\right)^2 + \sum_{i=1}^{3}\left(\frac{\partial H(\nu)}{\partial R_i}B_{R_i}\right)^2 + \left(\frac{\partial H(\nu)}{\partial p_s}B_{p_s}\right)^2 + \left(\frac{\partial H(\nu)}{\partial T_s}B_{T_s}\right)^2\right],$$

$$P_{H(\nu)}{}^2 = \left[\sum_{i=1}^{3}\left(\frac{\partial H(\nu)}{\partial L_i}P_{L_i}\right)^2 + \sum_{i=1}^{3}\left(\frac{\partial H(\nu)}{\partial R_i}P_{R_i}\right)^2 + \left(\frac{\partial H(\nu)}{\partial p_s}P_{p_s}\right)^2 + \left(\frac{\partial H(\nu)}{\partial T_s}P_{T_s}\right)^2\right],$$

with

$$U_{H(\nu)} = \left(B_{H(\nu)}{}^2 + P_{H(\nu)}{}^2\right)^{1/2},$$

where amplitude- and phase-response uncertainty is given by $\left|H(\nu) \pm U_{H(\nu)}\right|$ and $\arg\left(H(\nu) \pm U_{H(\nu)}\right)$ respectively. Consider the situations where:

1. Uncertainties in tube dimensions are unknown and only p_s and T_s uncertainty components are known, shown in Fig. 7 and Table 3;

2. Uncertainties in each variable are doubled, shown in Fig. 8 and Table 4.

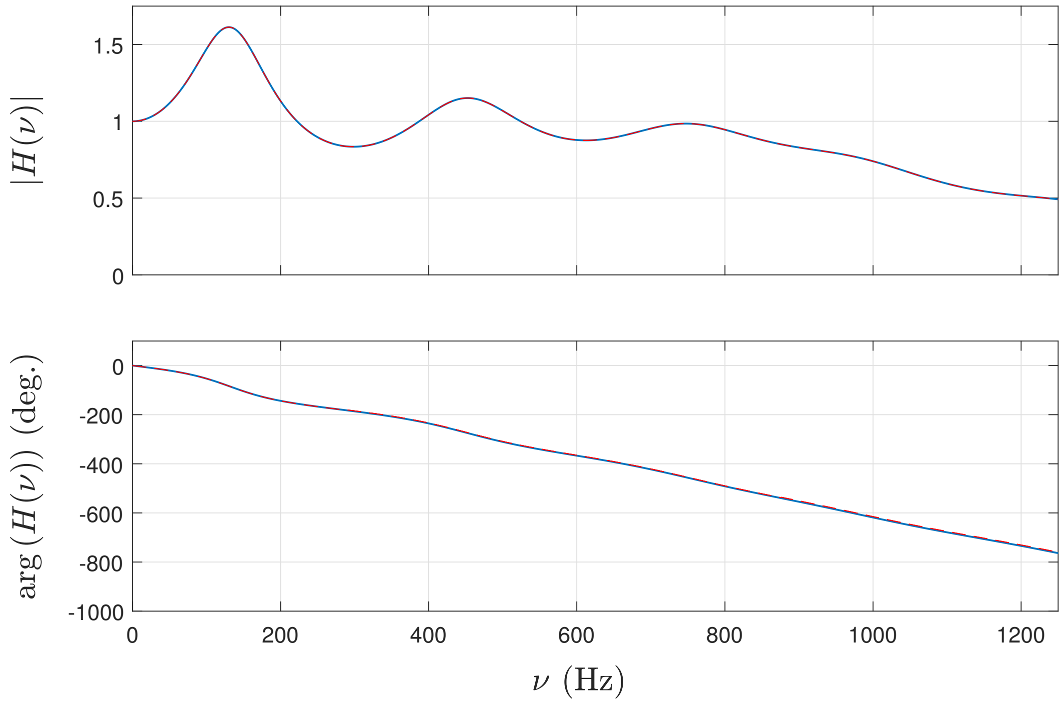

Figure 7: (– –) Total uncertainty at 95% confidence in (—) amplitude and phase responses, due to uncertainties in p_s and T_s only, as a function of ν for case-study I.

Table 3: Total uncertainty bounds at 95% confidence in amplitude and phase responses, due to uncertainties in p_s and T_s only, at discrete values of ν for case-study I.

ν (Hz)	$\lvert H(\nu)\rvert$	$\lvert H(\nu)+U_{H(\nu)}\rvert$ $\lvert H(\nu)-U_{H(\nu)}\rvert$	$\arg(H(\nu))$ (deg.)	$\arg(H(\nu)+U_{H(\nu)})$ $\arg(H(\nu)-U_{H(\nu)})$ (deg.)
250	0.896	0.895 0.896	−167.24	−167.24 −167.23
500	1.070	1.071 1.069	−310.19	−310.21 −310.18
1000	0.740	0.741 0.740	−618.44	−618.46 −618.41

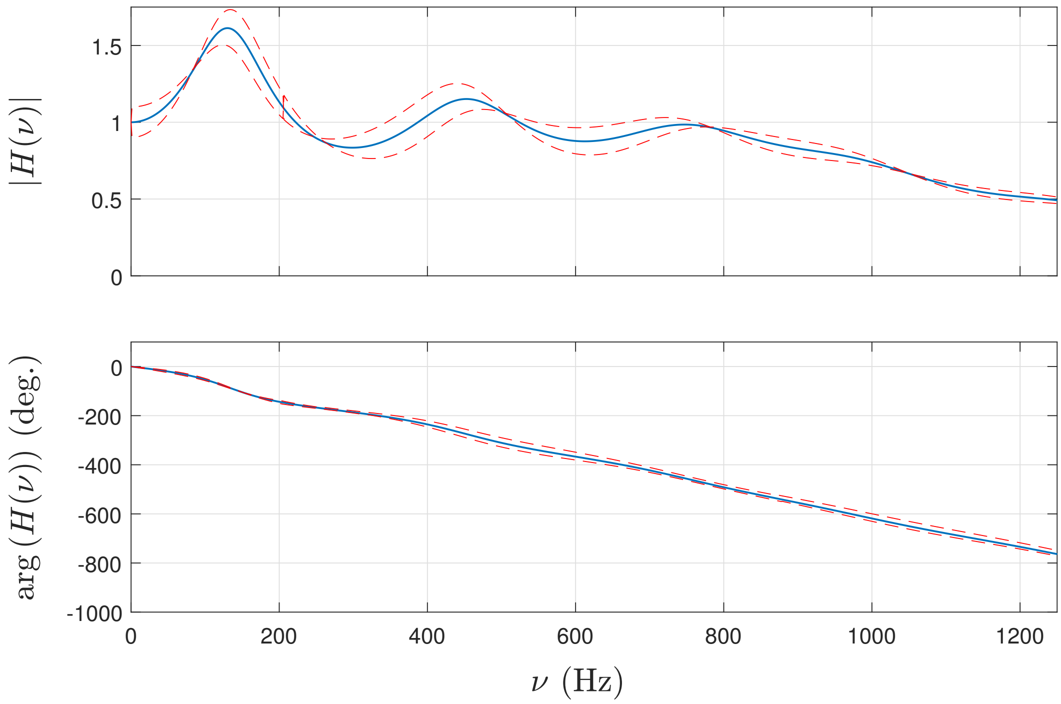

Figure 8: (– –) Total uncertainty at 95% confidence in (—) amplitude and phase responses, due to doubled uncertainties in L_j, R_j, p_s and T_s, as a function of ν for case-study I.

Table 4: Total uncertainty bounds at 95% confidence in amplitude and phase responses, due to doubled uncertainties in L_j, R_j, p_s and T_s, at discrete values of ν for case-study I.

ν (Hz)	$\lvert H(\nu)\rvert$	$\lvert H(\nu)+U_{H(\nu)}\rvert$ $\lvert H(\nu)-U_{H(\nu)}\rvert$	$\arg(H(\nu))$ (deg.)	$\arg(H(\nu)+U_{H(\nu)})$ $\arg(H(\nu)-U_{H(\nu)})$ (deg.)
250	0.896	0.914 0.901	−167.24	−157.88 −176.73
500	1.070	1.067 1.087	−310.19	−316.54 −303.97
1000	0.740	0.718 0.765	−618.44	−621.28 −615.76

Table 5: The effects of transfer-function uncertainty on the output signal for case-study I.

Signal	**RMS value**	**Phase lag (ms)**
$y(t)$	0.0403	–
Modulated $y(t)$	0.0470	0.8
Modulated $y(t)$ upper 95% confidence bound	0.0478	0.8
Modulated $y(t)$ lower 95% confidence bound	0.0463	0.8

Situation 1 represents a scenario where uncertainties in tube dimensions are not taken into account in the planning phase of an experimental test programme involving unsteady pressure measurements through tubes. Situation 2 is indicative of where there may be overly conservative estimates of variable uncertainties. It is clear that in both situations, amplitude and phase uncertainty bounds have changed somewhat proportionally to the changes in L_j, R_j, p_s and T_s uncertainties. Thus, the inaccurate assessments of uncertainties in L_j, R_j, p_s and T_s for situations 1 and 2 results in misrepresentations of overall uncertainty in the transfer function.

4.3.3. Effects of Transfer Function Uncertainty on Output Signal

Transfer-function uncertainty manifests as uncertainty in the unsteady component of the output signal (Eq. 1). A common method by which to report the unsteady component of the signal is using the standard deviation of the signal over time (e.g. [13]), which is also mathematically equivalent to the zero-mean RMS (as done in other published works, e.g. [10, 12]). A summary of the effects of transfer-function uncertainty on the output signal is given in Table 5. In order to report the confidence bounds of the RMS value of the predicted (or corrected) signal due to the transfer-function uncertainty, the following methodology is employed:

1. Calculate the RMS of the unsteady component of the predicted/corrected signal;

2. Take the upper confidence bound $H(\nu) + U_{H(\nu)}$ (which consists of N points), convolute it with the input signal, truncate the convoluted signal to the length of the input signal, and calculate the RMS value[6];

3. Same as above, but with the lower confidence bound $H(\nu) - U_{H(\nu)}$ in the convolution;

4. Calculate the differences between the RMS of the predicted/corrected signal, and the RMS values obtained from steps 2 and 3 respectively; the resultant values constitute the confidence bounds due to transfer-function uncertainty.

Following this methodology for the input signal $y(t)$ and derived transfer function $H(\nu)$ in this case study, the uncertainty in the output signal RMS value, due to transfer-function uncertainty, is about 0.0470 ± 0.0007. Additionally, by cross-correlating the input signal with the nominal and upper/lower confidence bound output signals, the uncertainty in phase lag is observed to be insignificant to within the selected quantisation (i.e. ν_s) of the input signal.

[6] N must be sufficiently large such that it does not affect the RMS result. In this case, $N = 2,048$ was found to be sufficient.

5. Case Study II: Measured Pressure Fluctuations on a Hemisphere

5.1. Overview

To further demonstrate the generalised method outlined in Section 3, representative data from a DST experimental test programme involving flow over a hemispherical protuberance are used in a transfer-function uncertainty analysis. In this test programme, the geometric constraints within the hemisphere, number of measurement locations, ability to measure both mean and unsteady pressure, as well as resolve the frequencies of interest all justified use of the DPMS rather than utilising individual unsteady pressure transducers.

One key parameter in these experiments was the RMS pressure coefficient over the hemisphere, defined as

$$(C_p)_{\mathrm{RMS}} = \frac{p_{\mathrm{RMS}}}{q_\infty}, \tag{35}$$

where p_{RMS} is the zero-mean RMS of the unsteady static pressure acting on the hemisphere surface, and $q_\infty = p_X - p_R$ is free-stream dynamic pressure measured two diameters above the hemisphere apex, using a pitot-static tube connected to two channels on the DPMS. Uncertainty in the amplitude response of the transfer function was considered to be more crucial, as it was shown previously in Table 5 that the phase uncertainty was negligible to within the quantisation of the input signal. Moreover, the DPMS corrects for the phase lag internally before outputting the pressure time series data to a file, so that the inter-channel measurements are considered to be quasi-simultaneous, see also [9].

5.2. Methodology Application and Results

Step 1 (Section 3.2.1) involves determining the tube configuration used in the experiments. The experiments consisted of a 100 mm diameter, aluminium hemisphere mounted onto a ground plane, which was installed into the DST Research Wind Tunnel (RWT). The hemisphere is hollow with a shell thickness of 2 mm, and there are 35 pressure taps spaced along the centreline meridian at 5° increments, with two additional taps located at 1° and 179°. Each pressure tap consists of a 20 mm long, 0.6 mm ID steel tube flush mounted with the hemisphere outer surface, see Fig. 9 for a photograph of the hemisphere pressure taps. Each tap was fitted with a flexible Scanivalve VINL-040 tube that is nominally 400 mm long and 0.86 mm ID, and it was ensured that the tubes were not kinked. The Scanivalve tubes connected each tap to a DPMS channel (Fig. 10), which has metallic tubing 60 mm long and 0.5 mm ID leading to a 3 mm^3 pressure transducer inside the chassis. The tube configuration for a single tap is shown in Fig. 11.

Step 2 (Section 3.2.2) involves derivation of the transfer function for the tube configuration. DPMS software is used to generate a theoretical transfer function to correct the measured pressure signals. A comparison of the transfer function generated using the DPMS software,

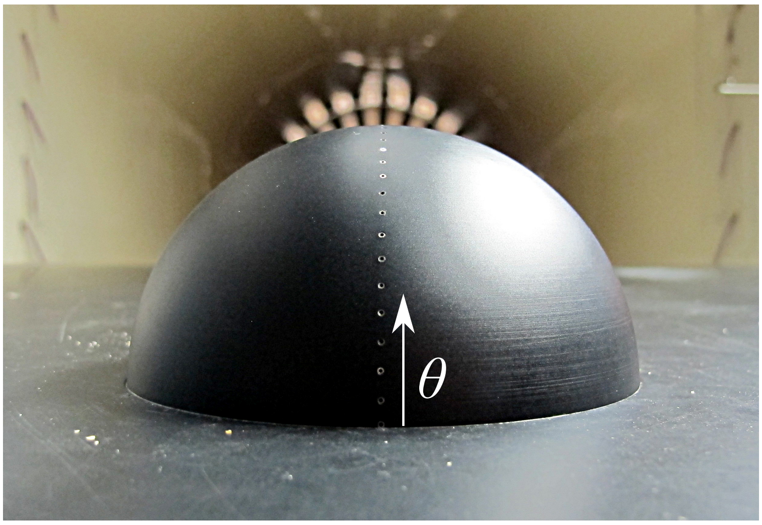

Figure 9: Hemisphere pressure taps with meridional angle θ shown. Note that the free-stream wind direction is into the page.

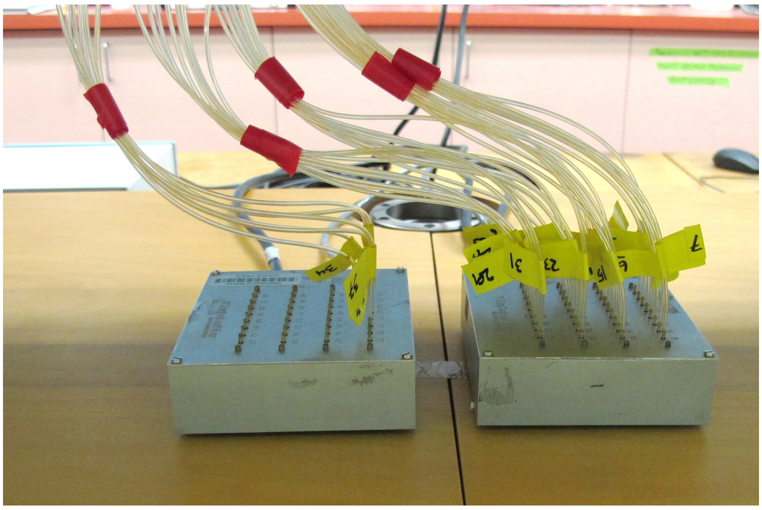

Figure 10: DPMS transducer channels connected to the hemisphere pressure taps (not shown) via flexible tubes.

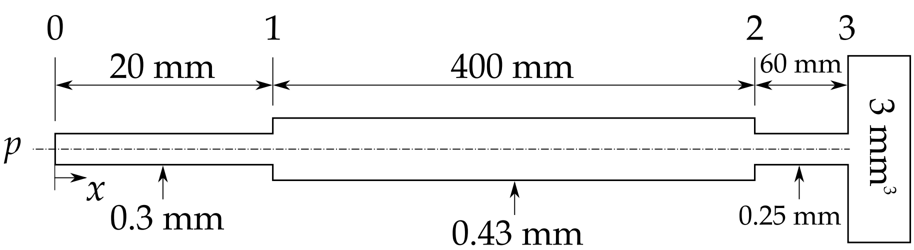

Figure 11: Tube configuration used in case-study II. Note that the diagram is not to scale.

and the one generated using the DST software tool (Appendix A), are shown in Fig. 12 for the experimental set-up at SSL conditions. The transfer functions are reasonably similar, with the only differences being that the DST software tool returns absolute phase response[7] as opposed to circular phase response where $-\pi \leq \text{phase} \leq \pi$ as in the DPMS software; also, the DPMS software accounts for the transfer function of an analogue Resistor-Capacitor (RC) low-pass filter within the unit [20], whereas the DST software tool does not. The surface pressure at each hemisphere tap was sampled at a rate of 2,500 Hz for a total sample period of 60 seconds. This meant that $\nu_c = 1,250$ Hz and since the amplitude response was about 0.5 at ν_c, the transfer function was used to correct pressure data up to and including the cut-off frequency.

Step 3 (Section 3.2.3) requires that all nominal values of each parameter are known. As per the first case study (Section 4), the DST software tool is utilised to determine nominal values in the domain of $0 < \nu \leq \nu_c$, for SSL conditions. The nominal values for the tubes are simply (Fig. 11);

$$L_1,\ L_2,\ L_3 = 20,\ 400,\ \text{and } 60 \text{ mm},$$
$$R_1,\ R_2,\ R_3 = 0.3,\ 0.43,\ \text{and } 0.25 \text{ mm},$$

from which V_{t_1}, V_{t_2} and V_{t_3} are calculated and $V_{v3} = 3$ mm^3 is obtained from the DPMS specifications.

Step 4 (Section 3.2.4) involves estimation of uncertainties in L_1, R_1 to L_3, R_3, p_s, and T_s using the method in Section 2.1, as well as DPMS transducer calibration data for uncertainties in pressure measurements [21]. All parameter uncertainties, as well as how they were estimated, are summarised in Table 6.

Steps 5 (Section 3.2.5) and *6* (Section 3.2.6) involve computing the sensitivity coefficients and ultimately calculating the transfer function uncertainty. These steps are performed identically to the first case study, with the uncertainty in amplitude and phase response for this tube configuration shown previously in Fig. 5. The RMS pressure coefficient, as a function of hemisphere centre-line meridional angle θ, is shown in Fig. 13 for a free-stream wind speed of 18.9 m/s.

5.3. Discussion

There are three distinct peaks in RMS pressure over the hemisphere, as can be seen in Fig. 13. The focus of this case study is not to analyse the physical flow phenomena occurring over the hemisphere; rather, it is suffice to say that these peaks have been observed elsewhere in published results [12, 13, 26]. The first peak at $\theta \approx 15°$ corresponds to the horseshoe vortex system present at the hemisphere upstream pole, while the peaks at $\theta \approx 85$ and $115°$ correspond to laminar and turbulent flow separation over the hemisphere, respectively.

The highlight of this discussion concerning Fig. 13 is the disparities between the magnitudes

[7] Absolute phase response, in this context, may be interpreted as a phase lag.

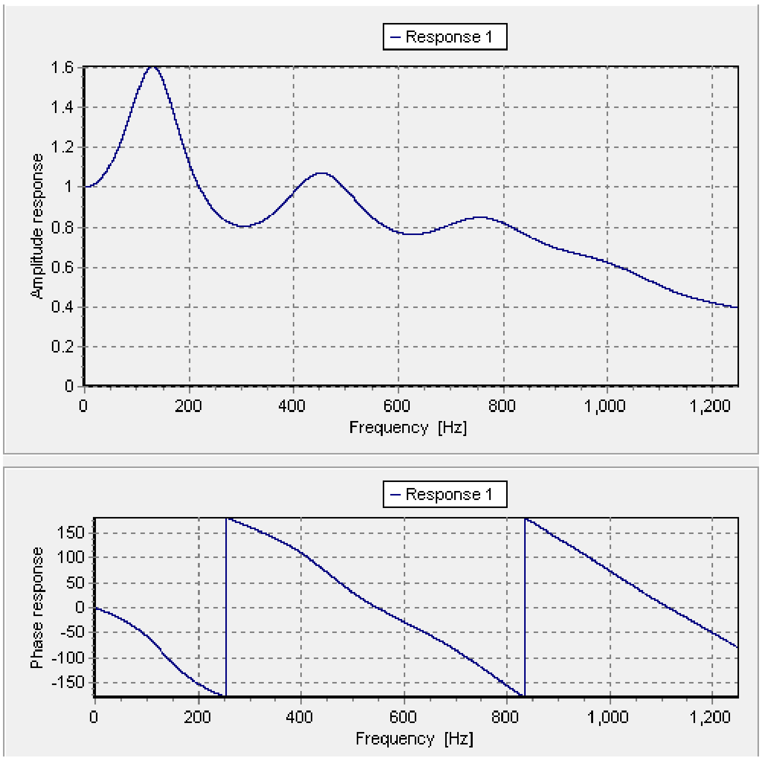

(i)

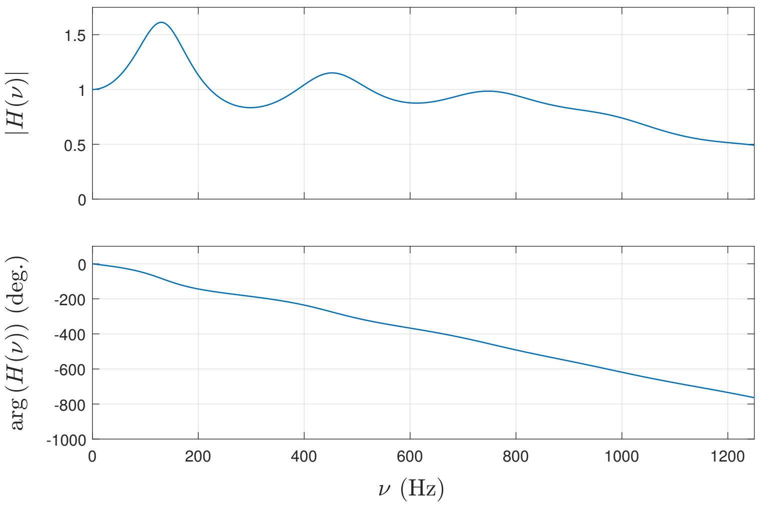

(ii)

Figure 12: (i) DPMS and (ii) DST software-based transfer function estimates to $\nu_c = 1,250$ Hz for case-study II.

Table 6: Estimated parameter uncertainties at 95% confidence with coverage factor $K = 2$ in case-study II.

Parameter	B_i	K, N_i	P_i	**Nominal Value**	**Estimation Method (B_i) (P_i)**
L_1 [mm]	±0.02	2, 20	±0.0256	20	Calliper calibration Eq. (6)
L_2 [mm]	±0.3	2, 37	±2	400	Steel rule tolerance [22] Conservative estimate
L_3 [mm]	±0.02	2, –	–	60	Assumed as L_1 –
R_1 [mm]	±0.0254	2, –	–	0.3	Manufacturer tolerance [23] –
R_2 [mm]	±0.1	2 ,–	–	0.43	Previous estimates [14] –
R_3 [mm]	±0.0254	2, –	–	0.25	Assumed as R_1 –
p_s [Pa]	±15	2, 60	±5.31	101,325	Transducer calibration [24] Eq. (6)
T_s [K]	±0.88	2, 60	±0.0231	288.15	Transducer calibration [25] Eq. (6)
$\langle p \rangle$, p_X, p_R [Pa]	±10.73	2, 150000	±0.745	DPMS channel dependent	DPMS calibration [21] Eq. (6)

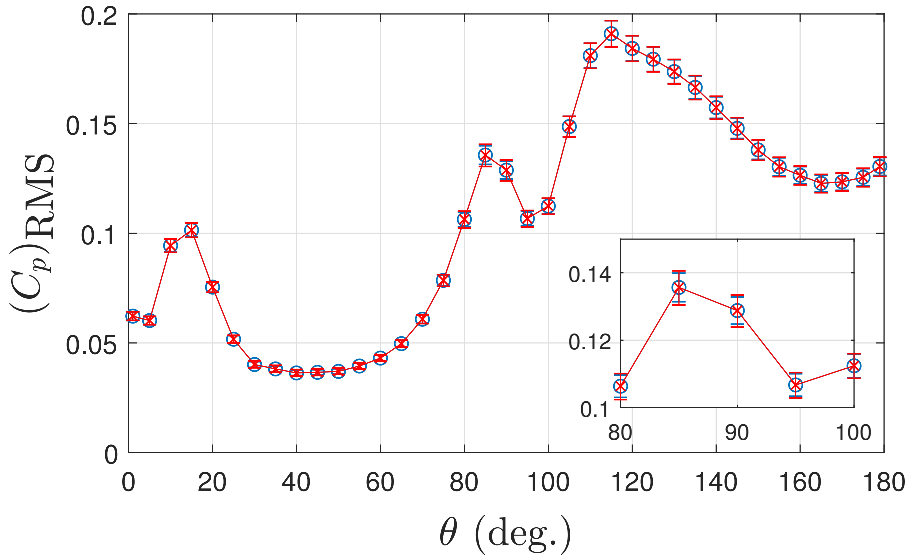

Figure 13: Uncertainty at 95% confidence in RMS pressure coefficient over the hemisphere: (—) considering only the DPMS transducer calibration [21], and (—) considering the RSS of the DPMS transducer calibration and transfer-function uncertainty, for case-study II. Inset: a magnified view of the second peak in RMS pressure coefficient.

of the uncertainty bounds. An uncertainty analysis was carried out on the same unsteady-pressure dataset, but using two different methods:

1. The blue data in Fig. 13 are the RMS pressure coefficient uncertainty, considering only the uncertainty in the DPMS transducer calibrations, obtained from a previous check-calibration of the system [21]. Note that this analysis accounts for the correlated bias uncertainties arising in the use of the DPMS for measuring p_{RMS} (which is $\langle p \rangle - \overline{p}$), p_X and p_R (Section 2.2).

2. The red data in Fig. 13 are the RMS pressure coefficient uncertainty, considering the RSS of the uncertainty due to the DPMS transducer calibration as well as the transfer-function uncertainty.

It is important to note that the measured pressure time series utilised in this case study were transfer-function corrected internally by the DPMS before being output to a file for post-processing. The DPMS transfer-function generator utilises a proprietary file format for the transfer function, such that the corrected data cannot be "de-corrected" using the same DPMS-generated transfer function[8]. Thus here, the corrected data output by the DPMS is DFT de-convoluted with the nominal transfer function generated by the DST software tool (Fig. 12ii) to return the de-corrected time series. This process does introduce slight inaccuracies due the aforementioned incongruence between the DPMS- and DST-software generated transfer functions (Section 5.2), but for the purposes of this case study these inaccuracies were considered

[8]However, it should be noted that DPMS data may be output to a file without being convoluted with the transfer function, if the user desires.

insignificant. The de-corrected data were then processed according to the methodology outlined in Section 4.3.3, to return the unsteady-pressure uncertainty bounds due to uncertainties in the transfer function parameters.

In general, it may be seen in Fig. 13 that there is an increase in $(C_p)_{\mathrm{RMS}}$ uncertainty for both estimation methods near the locations of the three peaks, which is expected behaviour given the increased pressure fluctuations at these locations. However, it is evident that there is a slightly larger uncertainty range over the dataset when the contribution from the transfer function is included in the uncertainty estimate, and also that there are asymmetrical uncertainty bounds at certain locations. Asymmetry in the $(C_p)_{\mathrm{RMS}}$ uncertainty bounds can occur depending on the spectral content of the measured signal, as well as the nature of the transfer-function uncertainty bounds $H(\nu) \pm U_{H(\nu)}$ as observed in the first case study (Section 4.3). For example, near the second peak at $\theta = 85°$, the uncertainty estimates including the transfer-function contribution are slightly larger than estimates where this contribution was neglected, and the 95% confidence interval is asymmetrically distributed about the nominal value of $(C_p)_{\mathrm{RMS}}$. In contrast, the transfer-function contribution to $(C_p)_{\mathrm{RMS}}$ uncertainty near $\theta = 115°$ is essentially negligible. This could indicate that the spectral contents of the measured signals at the second and third peaks (i.e. $\theta = 85$ and $115°$ respectively) interact differently with the transfer-function uncertainty bounds, as a function of ν, through convolution. These results demonstrate a physical dependence of the overall uncertainty on the nature of the pressure fluctuations, when measured through tubes.

Uncertainty estimations in measurements should ideally account for uncertainties in all system parameters—and if not all parameters, then certainly the most crucial ones [2]. The disparities observed between the data uncertainties in Fig. 13 occur because uncertainties in the DPMS transducer calibrations, even though here are the dominant source of uncertainty, are still an incomplete descriptor of the overall uncertainty when measuring the pressure fluctuations through tubes. The tubes modulate the physics of the measured pressure fluctuations and thus uncertainty estimations must reflect this modulation; otherwise the overall uncertainty in fluctuating pressure may be misrepresented, as evinced in this case study. More importantly, the extent to which the transfer-function uncertainty affects the fluctuating pressure uncertainty is likely dependent upon the tube configuration (e.g. see Fig. 6), which is unique to each test depending on measurement requirements. Altogether, misrepresentation of the overall uncertainty results in data inferences based on inaccurate uncertainty estimations in the system, potentially leading to over-interpretation of data trends and fallible conclusions.

6. Conclusions

A general method by which to quantify uncertainty in theoretical corrections to unsteady pressure measurements through N_t tubes and N_v volumes has been presented in this report. This method is based on the well-validated theoretical model in [1] and is in accordance with AIAA Standards for quantifying uncertainty in wind-tunnel measurements [2]. Specifically, this method may be used to formally propagate uncertainties in tube dimensions and mean ambient conditions into the estimation of uncertainty in measured pressure fluctuations through tubes, when using a theoretical transfer function to correct the data. Aided by two separate case studies and a DST-developed software tool, it has been shown that:

1. Amplitude-response uncertainty is highly sensitive to uncertainties in tube dimensions and moderately sensitive to mean ambient conditions.

2. Phase-response uncertainty is chiefly influenced by the relative magnitudes of uncertainties in tube dimensions and mean ambient conditions.

3. Uncertainty in both amplitude and phase response at a given frequency is dependent upon the response characteristic of the tube configuration at that frequency.

4. Neglecting the transfer-function contribution may lead to a misrepresentation of the overall uncertainty estimate in pressure fluctuations, depending on the spectral content of the measured signal or tube configuration.

7. Recommendations

Quantifying uncertainty in measurements is required for quality assurance. The theory developed by Bergh & Tijdeman [1] may be utilised to provide a rapid yet accurate correction to unsteady pressure measurements through tubes, but the complicated nature of uncertainty in the theoretical transfer function has been demonstrated in this report. In light of these findings, the following recommendations are made:

1. The use of tubes between the pressure-disturbance source and pressure transducer be avoided if possible. If tubes are unavoidable, or deemed necessary, then

2. An experimental calibration of the pressure measurement system and tubing configurations be done to obtain experimental transfer functions. In this way, the transfer functions are devoid of uncertainties in L_j and R_j, but still subject to uncertainties in p_s and T_s. If an experimental calibration is not feasible, then

3. The methodology in this report be carried out in the planning phase of an experimental test programme, such that the effect of L_j, R_j p_s and T_s uncertainties, as well as tube configuration, on the uncertainty of theoretical corrections is appreciated *a priori* to measurements.

4. Further investigative work be carried out to determine uncertainty-reduction strategies.

8. References

[1] Bergh, H. & Tijdeman, H. (1965) *Theoretical and Experimental Results for the Dynamic Response of Pressure Measuring Systems*, Technical report, National Aerospace Laboratory.

[2] AIAA (1999) Assessment of experimental uncertainty with application to wind tunnel testing, Standard No. AIAA S-071A.

[3] Kulite (2017) *Pressure Transducer Handbook*, Technical report, Kulite Semiconductor Products, Inc., Leonia, NJ, USA.

[4] Irwin, H. P. A. H., Cooper, K. R. & Girard, R. (1979) Correction of distortion effects caused by tubing systems in measurements of fluctuating pressures, *Journal of Industrial Aerodynamics* **5**, 93 – 107.

[5] Holmes, J. D. & Lewis, R. E. (1987) Optimization of dynamic pressure-measurement systems: I: single-point measurements, *Journal of Wind Engineering and Industrial Aerodynamics* **25**, 249 – 273.

[6] Hooper, J. D. & Musgrave, A. R. (1997) Mean velocity, static and dynamic pressure measurement by a four-hole pressure probe, *Experimental Thermal and Fluid Science* **15**, 375 – 383.

[7] Mousley, P., Watkins, S. & Hooper, J. (1998) Use of a hot-wire anemometer to examine the pressure signal of a high-frequency pressure probe, *in 13th Australian Fluid Mechanics Conference*, Monash University, Melbourne, Australia.

[8] Levinski, O., Hill, B. A. & Watmuff, J. (2007) Experimental investigation of vertical tail buffet, *in Australian International Aerospace Congress, AIAC12*, number 38.

[9] Levinski, O. (2012) Application of dynamic pressure measurement for empennage buffet, *in 28th International Congress of the Aeronautical Sciences, ICAS2012*.

[10] McCarthy, J., Giacobello, M. & Lam, S. (2019) Wavelet coherence of surface pressure fluctuations due to von Kármán vortex shedding near a hemispherical protuberance, *Experiments in Fluids* **60**(3), 1 – 13.

[11] McCarthy, J. & Lee, S.-K. (2018) Wavelet coherence analysis of fluctuating surface pressure on a hemispherical protuberance, *in 21st Australasian Fluid Mechanics Conference*, Adelaide, Australia.

[12] Cheng, C. & Fu, C. (2010) Characteristic of wind loads on a hemispherical dome in smooth flow and turbulent boundary layer flow, *Journal of Wind Engineering and Industrial Aerodynamics* **98**, 328 – 344.

[13] Taylor, T. (1992) Wind pressures on a hemispherical dome, *Journal of Wind Engineering*

and Industrial Aerodynamics **40**(2), 199 – 213.

[14] Fisher, A. M. (2013) *The effect of freestream turbulence on fixed and flapping micro air vehicle wings*, PhD thesis, School of Aerospace, Mechanical and Manufacturing Engineering, RMIT University, Melbourne, Australia.

[15] Gordon, S. & McBride, B. J. (1994) *Computer Program for Calculation of Complex Chemical Equilibrium Compositions and Applications*, Reference Publication 1311, National Aeronautics and Space Administration.

[16] Stephan, K. & Laesecke, A. (1985) The thermal conductivity of fluid air, *Journal of Physical Chemistry Reference Data*.

[17] Sutherland, W. (1893) The viscosity of gases and molecular force, *Philosophical Magazine* **5**(36), 507 – 531.

[18] Levinski, O. (2017) Pers. Comm.

[19] Smith, S. W. (1997) *The Scientist and Engineer's Guide to Digital Signal Processing*, California Technical Publishing, San Diego, California.

[20] Mousley, P. (2018) Pers. Comm.

[21] McCarthy, J. (2018) *Static Check-Calibration of a Dynamic Pressure Measurement System: Serial Numbers DPM1201 and DPM1203*, Technical Note DST-Group-TN-1821, Aerospace Division, Defence Science and Technology, 506 Lorimer Street, Fishermans Bend, VIC 3207.

[22] Toledo (2018) *Measuring and Precision*.

[23] VitaNeedle (2018) Hypodermic tube gauge chart, URL: <https://www.vitaneedle.com/hypodermic-tube-gauge-chart/>, accessed 29/06/2018.

[24] Vaisala (2016) *PTB110 Barometer Calibration Certificate*, Calibration Report H47-16460020, Vaisala Oyj, PO Box 26, FI-00421 Helsinki, Finland.

[25] LabJack (2017) EI-1034 Datasheet, URL: <http://www.labjack.com/>, accessed 21/12/2017.

[26] Fedrezzi, M. (2012) Flow over a hemisphere in a flat plate boundary layer, Final Year Thesis. Monash University Laboratory for Turbulence Research in Aerospace and Combustion.

This page is intentionally blank

Appendix A. Software Tool

A.1. Description

In order to assess transfer-function uncertainty with respect to uncertainties in variables L_j, R_j, p_s and T_s, a simple software tool written in Python programming language was developed at DST. The software currently[9] operates as a Command-Line Interface (CLI) and prompts the user for information relating to the transfer function as well as uncertainties in variables. At its core, the program utilises the NumPy module[10]—which is used for array-based operations, and the SymPy module[11], which is a symbolic mathematics engine.

The software tool evaluates the sensitivity coefficients of the transfer function *exactly* using symbolic mathematical operations, rather than relying on a numerical differentiation scheme. Though slower, exact partial differentiation avoids dependence on the type of numerical differentiation scheme as well as discrete step sizing. The integration of NumPy and SymPy environments within Python enable partially differentiated symbolic expressions to be subsequently numerically evaluated using array-based operations, thus permitting the transfer function uncertainty to be assessed as a function of ν.

While the software tool may be readily upgraded and expanded in capability, the current version of the software has the following functionalities:

- Calculate the nominal transfer function for an N_t-tube, single-volume configuration.
- Optionally calculate uncertainties in amplitude and phase responses, given uncertainties in variables L_j, R_j, p_s and T_s.
- Plot the nominal amplitude and phase responses in a separate window for visualisation and saving, if required. If an uncertainty analysis was conducted, also plot uncertainty bounds at 95% confidence about the nominal amplitude and phase responses.
- Output results to a Comma Separated Value (*.csv) file, with header text containing all tube dimensions, ambient conditions, and uncertainty information.
- Output the transfer function and uncertainty arrays to a MATLAB workspace file (*.mat), to allow for convolution with unsteady-pressure time series data in the MATLAB environment.

A.2. Known Limitations

The current version of the software has limitations regarding the nature of the uncertainty analysis, as well as software compatibility and runtime. The following list of limitations is not exhaustive, and other limitations may exist:

[9] Proposed upgrades are noted in Section A.3.
[10] `https://docs.scipy.org/doc/numpy/index.html`
[11] `http://docs.sympy.org/latest/index.html`

- Correlated bias uncertainties are not considered in the uncertainty analysis.
- The machine on which this software is executed must have Python, NumPy and SymPy installed.
- The software has been tested and subsequently used on a machine with Python version 3.6.5, NumPy version 1.14, and SymPy version 1.01. It is currently unknown whether previous versions of Python, NumPy or SymPy will execute properly, or reproduce results from the current version.
- Unrealistically large values of L_j or R_j cause numerical overflow errors in the SymPy module. The precise thresholds of these values are currently unknown, but the software will crash if overflow occurs.
- Larger N_t, and/or a larger number of DFT points will cause a significant decrease in execution speed if an uncertainty analysis is done, as the software must exactly evaluate increasingly complicated partial derivatives and/or a larger number of DFT points.

A.3. Potential Upgrades

In order to facilitate more general use of the software tool, the following future upgrades are suggested:

- Develop a Graphical User Interface (GUI) to enclose the core software capability.
- Perform an analysis for an N_t-tube, N_v-volume configuration.
- Optimise code for efficient execution.

A.4. Software Flowchart

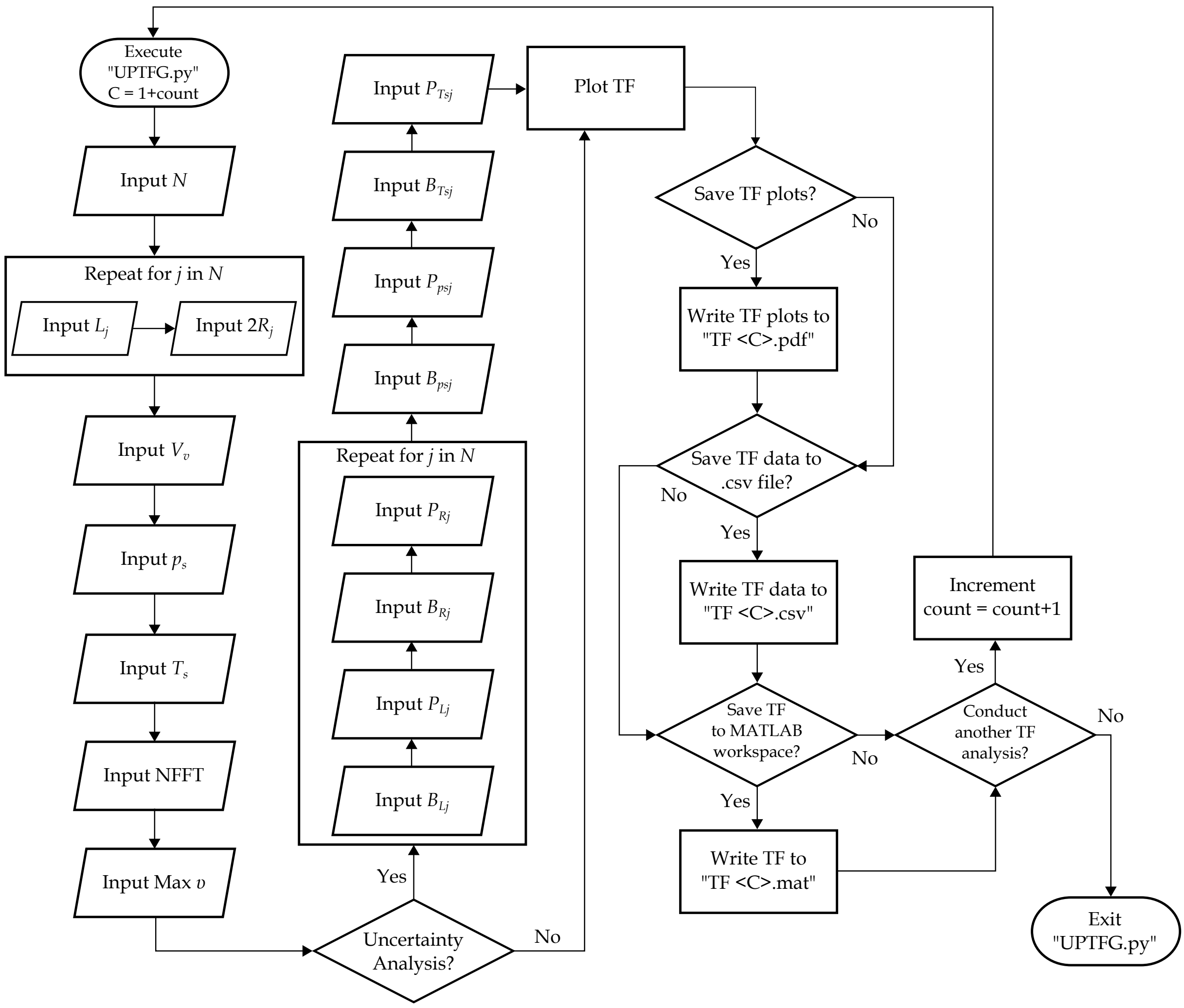

Figure 14: DST software-tool logic flowchart.

This page is intentionally blank

DEFENCE SCIENCE AND TECHNOLOGY GROUP DOCUMENT CONTROL DATA	1. DLM/CAVEAT (OF DOCUMENT)

2. TITLE	3. SECURITY CLASSIFICATION (FOR UNCLASSIFIED LIMITED RELEASE USE (L) NEXT TO DOCUMENT CLASSIFICATION)
The Estimation of Uncertainty in Theoretical Corrections to Unsteady Pressure Measurements through Tubes	Document (U) Title (U) Abstract (U)
4. AUTHORS	5. CORPORATE AUTHOR
Jesse McCarthy and Malcolm Jones	Defence Science and Technology Group 506 Lorimer St, Fishermans Bend, Victoria 3207, Australia

6a. DST GROUP NUMBER	6b. AR NUMBER	6c. TYPE OF REPORT	7. DOCUMENT DATE
DST-Group–TR–3579		Technical Report	June, 2019

8. OBJECTIVE ID	9. TASK NUMBER	10. TASK SPONSOR

11. MSTC	12. STC
Aircraft Performance and Survivability	Aerodynamics and Flight Mechanics
13. DOWNGRADING/DELIMITING INSTRUCTIONS	14. RELEASE AUTHORITY
	Chief, Aerospace Division

15. SECONDARY RELEASE STATEMENT OF THIS DOCUMENT

Approved for Public Release

OVERSEAS ENQUIRIES OUTSIDE STATED LIMITATIONS SHOULD BE REFERRED THROUGH DOCUMENT EXCHANGE, PO BOX 1500, EDINBURGH, SA 5111

16. DELIBERATE ANNOUNCEMENT

No Limitations

17. CITATION IN OTHER DOCUMENTS

No Limitations

18. RESEARCH LIBRARY THESAURUS

Pressure measurement, Uncertainty analysis, Dynamic characteristics, Wind tunnel tests

19. ABSTRACT

A general method used to quantify uncertainty in theoretical corrections to unsteady pressure measurements through tubes is documented in this report. This method is based on a well-validated theoretical model, which produces a transfer function that may be used for correcting unsteady pressure measurements through an N_t number of tubes and N_v number of volumes. The uncertainty estimation methods employed are in accordance with AIAA Standards. A software tool, implementing a synthesis of the theoretical model and AIAA uncertainty estimation methodology, is also developed in this work. Aided by two separate case studies, it is found that by failing to account for uncertainty in the transfer function that is used to correct unsteady pressure data, the overall uncertainty in measured unsteady pressure may be misrepresented, depending on the spectral content of the measurements or tube configuration.